Article

Cell

# iPSCs from a Hibernator Provide a Platform for Studying Cold Adaptation and Its Potential Medical Applications

## Graphical Abstract

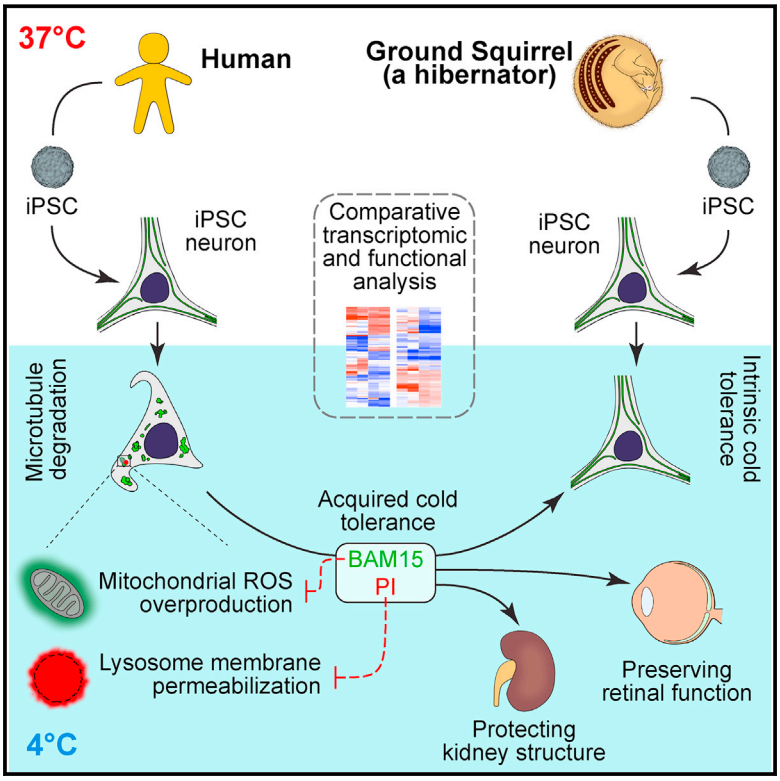


## Highlights

- iPSCs made from a hibernator (13-lined ground squirrel, *Ictidomys tridecemlineatus*)
- Ground squirrel (GS) iPSC-differentiated neurons retain intrinsic cold resistance
- Human and GS neurons differ in their mitochondrial and lysosomal responses to cold
- Drugs targeting these pathways improve cold tolerance in non-hibernator cells

## Authors

Jingxing Ou, John M. Ball, Yizhao Luan, ..., Zhi Xie, Barbara S. Mallon, Wei Li

## Correspondence

liwei2@nei.nih.gov

## In Brief

iPSC-derived neurons from the 13-lined ground squirrel, a hibernator, allow investigation of cellular cold resistance with implications for improved cold storage for organ transplants.

Ou et al., 2018, Cell *173*, 1–13
May 3, 2018 Published by Elsevier Inc.
https://doi.org/10.1016/j.cell.2018.03.010

CellPress

Please cite this article in press as: Ou et al., iPSCs from a Hibernator Provide a Platform for Studying Cold Adaptation and Its Potential Medical Applications, Cell (2018), https://doi.org/10.1016/j.cell.2018.03.010



Cell

# iPSCs from a Hibernator Provide a Platform for Studying Cold Adaptation and Its Potential Medical Applications

Jingxing Ou,[1] John M. Ball,[1,9] Yizhao Luan,[2,3,9] Tantai Zhao,[1,4,9] Kiyoharu J. Miyagishima,[1,9] Yufeng Xu,[1,5,9] Huizhi Zhou,[6] Jinguo Chen,[6] Dana K. Merriman,[7] Zhi Xie,[2] Barbara S. Mallon,[8] and Wei Li[1,10,*]

[1]Retinal Neurophysiology Section, National Eye Institute, National Institutes of Health, Bethesda, MD 20892, USA
[2]State Key Laboratory of Ophthalmology, Guangdong Provincial Key Lab of Ophthalmology and Visual Science, Zhongshan Ophthalmic Center, Sun Yat-sen University, Guangzhou 510060, China
[3]School of Life Sciences, Sun Yat-sen University, Guangzhou 510275, China
[4]Department of Ophthalmology, The Second Xiang-Ya Hospital, Central South University, Changsha 410011, China
[5]Department of Ophthalmology, The Second Affiliated Hospital of Zhejiang University, College of Medicine, Hangzhou 310009, China
[6]Trans-NIH Center for Human Immunology, Autoimmunity, and Inflammation, National Institutes of Health, Bethesda, MD 20892, USA
[7]Department of Biology, University of Wisconsin, Oshkosh, WI 54901, USA
[8]NIH Stem Cell Unit, National Institute of Neurological Disorders and Stroke, National Institutes of Health, Bethesda, MD 20892, USA
[9]These authors contributed equally
[10]Lead Contact
*Correspondence: liwei2@nei.nih.gov
https://doi.org/10.1016/j.cell.2018.03.010

## SUMMARY

**Hibernating mammals survive hypothermia (<10°C) without injury, a remarkable feat of cellular preservation that bears significance for potential medical applications. However, mechanisms imparting cold resistance, such as cytoskeleton stability, remain elusive. Using the first iPSC line from a hibernating mammal (13-lined ground squirrel), we uncovered cellular pathways critical for cold tolerance. Comparison between human and ground squirrel iPSC-derived neurons revealed differential mitochondrial and protein quality control responses to cold. In human iPSC-neurons, cold triggered mitochondrial stress, resulting in reactive oxygen species overproduction and lysosomal membrane permeabilization, contributing to microtubule destruction. Manipulations of these pathways endowed microtubule cold stability upon human iPSC-neurons and rat (a non-hibernator) retina, preserving its light responsiveness after prolonged cold exposure. Furthermore, these treatments significantly improved microtubule integrity in cold-stored kidneys, demonstrating the potential for prolonging shelf-life of organ transplants. Thus, ground squirrel iPSCs offer a unique platform for bringing cold-adaptive strategies from hibernators to humans in clinical applications.**

## INTRODUCTION

Hibernation in mammals is a seasonal state of metabolic suppression and dormancy characterized by a decrease in body temperature (Andrews, 2007; Barnes, 1989; Carey et al., 2003; Geiser, 2004). Small hibernators such as 13-lined ground squirrels (GS; *Ictidomys tridecemlineatus*) use this remarkable strategy to survive extreme environmental stresses (Drew et al., 2007; Staples, 2016; Storey and Storey, 2010). They routinely withstand a body temperature below 10°C that would otherwise cause severe injuries and organ failure in non-hibernating mammals (Quinones et al., 2014). For example, GS platelets display resistance to cold-storage-induced damage (Cooper et al., 2012), and GS kidney tubular cells exhibit significantly less cell death when subjected to cold storage/rewarming compared to mice (Jain et al., 2016). If the mechanisms underlying such cold tolerance could be reproduced in non-hibernators, it would hold great promise for clinical applications.

Indeed, even with a mild temperature drop (2°C–3°C below normal body temperature), induced hypothermia has been shown to promote patient survival in critical-care situations (Delhaye et al., 2012; Yenari and Han, 2012). At this temperature range, cold-shock proteins (e.g., RBM3 and CIRP) are induced, which demonstrate promising neuroprotective effects (Bastide et al., 2017; Peretti et al., 2015; Zhu et al., 2016). However, hibernating GSs, whose body temperature drops from normal (~37°C) to near freezing for days at a time, confront a much more strenuous challenge and yet avoid neurological damage (Arendt et al., 2003; von der Ohe et al., 2006). The mechanisms involved in cold adaptation at such hibernation-like temperatures remain unclear. One critical vulnerability is that the microtubule cytoskeleton quickly depolymerizes at near-freezing temperatures (Breton and Brown, 1998; Wallin and Strömberg, 1995; Weber et al., 1975). Microtubules have various cellular functions and are vital to many organs and the nervous system, as neurons require a stable microtubule cytoskeleton to maintain their elaborate dendritic and axonal processes as well as proper synaptic connections (Conde and Cáceres, 2009; Kapitein and Hoogenraad, 2015; Penazzi et al., 2016). Hence, failure to protect the

microtubules would result in catastrophic functional impairment. Although microtubule-associated proteins (MAPs) can facilitate short-term (~1 h) microtubule stability in neurons at ~4°C (Bosc et al., 2003; Guillaud et al., 1998; Webb and Wilson, 1980), how GSs maintain their microtubules in days-long hibernation bouts remains a mystery. Understanding the mechanisms of such remarkable cold adaptations during hibernation will be vital for harnessing the benefit of metabolic regulation and avoiding the harmful effects of such low temperatures (Dave et al., 2012; Forreider et al., 2017; Nathaniel, 2008).

In recent years, systematic profiling approaches have unveiled unique features of hibernators at gene and protein levels (Fedorov et al., 2014; Hampton et al., 2013; Hindle and Martin, 2013; Morin and Storey, 2009; Williams et al., 2005). However, hibernating species such as GSs are non-conventional animal models with annual reproductive cycles that hinder access to early developmental tissues. Consequently, hibernation research at molecular and cellular levels has been impeded by both a lack of transgenic models for *in vivo* genetic manipulations and a limited choice of cell types (Drew et al., 2011) for *in vitro* studies. To this end, induced pluripotent stem cells (iPSCs) (Takahashi and Yamanaka, 2006) are a valuable alternative that can establish various cell types and tissue models for in-depth mechanistic studies *in vitro*.

Here, we report for the first time the establishment of iPSCs from a hibernating mammal (GS) to study their hibernation-specific features, inspiring novel pharmacological strategies to bestow cold adaptability to cells and organs from non-hibernating mammals. We found that neurons differentiated from GS iPSCs retain intrinsic cold-resistant features such as microtubule stability. This enabled us to identify cellular pathways linking mitochondria-initiated oxidative stress and dysfunctional lysosomes with microtubule instability in the cold. Using drugs targeting these pathways, we demonstrate that human iPSC-derived neurons (iPSC-neurons) and rat retinal neurons can acquire cold-resistant features. Remarkably, these treatments functionally rescued cold-exposed rat retinal tissues whose structure and function would otherwise have been compromised. Furthermore, the same treatments prevented cold-induced microtubule and other damage in mouse kidneys undergoing conventional transplantation storage. Prospectively, GS iPSCs can serve as a valuable platform for exploring the unique mechanisms of metabolic adaptation and stress responses in hibernators and for facilitating the translation of hibernation research to medical applications.

## RESULTS

### GS iPSC-Neurons Recapitulate the Intrinsic Cold Resistance of Native GS Neurons

We first compared neuronal microtubule morphology from GSs and rats (a non-hibernator) at 4°C using antibodies against the neuron-specific β-tubulin isotype-III (TUBB3) and two α-tubulin isotypes that are enriched in neurons (Δ2-T, poly-E-T). At physiological temperatures (37°C), rat neurons contained long, smooth microtubule processes; however, a 4-hr incubation at 4°C induced microtubule fragmentation. Moreover, following an extended 16-hr incubation at 4°C, most rat neuron microtubules disappeared, leaving abnormal tubulin aggregates (Figure 1A). Human iPSC-neurons exhibited similar cold-induced microtubule instability (Figure 1B). In stark contrast, cortical neurons cultured from neonatal GSs showed no signs of deterioration even after 16 hr of cold exposure (Figure 1C).

To overcome the limited accessibility of primary cultures of GS neurons and to facilitate mechanistic studies of microtubule cold resistance *in vitro*, we established GS iPSC lines from neonatal GS cortex using a modified reprogramming protocol and validated their pluripotency (Figures S1A–S1C). As with GS cortical primary neurons, microtubules of GS iPSC-neurons showed little difference between 37°C and 4°C incubations for 16 hr (Figures 1D and 1E), suggesting that GS iPSC-neurons retain endogenous cold resistance.

### Species-Specific Gene Expression Profiles Highlight Cellular Pathways that Contribute to Microtubule Destruction in the Cold

To elucidate how GS neurons preserve their microtubule integrity in the cold, we first examined tubulin protein expression. In agreement with microtubule morphology, protein levels of TUBB3, poly-E-T, and Δ2-T remained unchanged in GS iPSC-neurons following 16-hr incubation at 4°C (Figure 2A). In contrast, in human iPSC-neurons following 4 hr at 4°C, tubulin protein levels were significantly reduced (Figure 2A). These observed changes in microtubule homeostasis were not a secondary phenomenon attributable to cell death (Figure S2A).

To test whether such microtubule destabilization resulted from a diminished pool of tubulin proteins, we overexpressed TUBB3 in human iPSC-neurons. *TUBB3* overexpression temporarily preserved expression of all three proteins (TUBB3, poly-E-T, and Δ2-T) and long neurites for 4-hr cold exposure (Figures 2A and S2D), likely by recruiting poly-E-T and Δ2-T to form more stable polymers. However, this rescue effect did not extend to the 16-hr group (Figure S2D), perhaps due to cessation of *TUBB3* production at 4°C and other cellular responses contributing to tubulin degradation.

We then used comparative RNA profiling in human and GS iPSC-neurons to systematically examine possible mechanisms of cold-induced tubulin degradation (Figure S3; Data S1, S2, and S3). Clustering analysis of differentially expressed genes (DEGs) and pathway analysis indicated that mitochondrial functions are among the most significantly changed pathways upon cold exposure (yellow cluster in Figure S3E and Data S2, and Figure S3F). Among these most significantly changed pathways, two function-related gene clusters showed distinctly changing patterns in GS and human iPSC-neurons during cold exposure: (1) mitochondria-related genes and (2) genes participating in protein quality control (PQC), including heat-shock proteins (HSPs), proteases, and proteinase inhibitor genes (Figures 2B and S3F). These differentially affected pathways prompted us to investigate whether the mitochondrial and PQC responses to cold exposure contribute to microtubule destruction in human iPSC-neurons.

### Cold Induces Mitochondrial Hyperpolarization and ROS Over-Production in Human iPSC-Neurons

To examine whether mitochondria in human and GS iPSC-neurons respond differently to cold exposure, we monitored

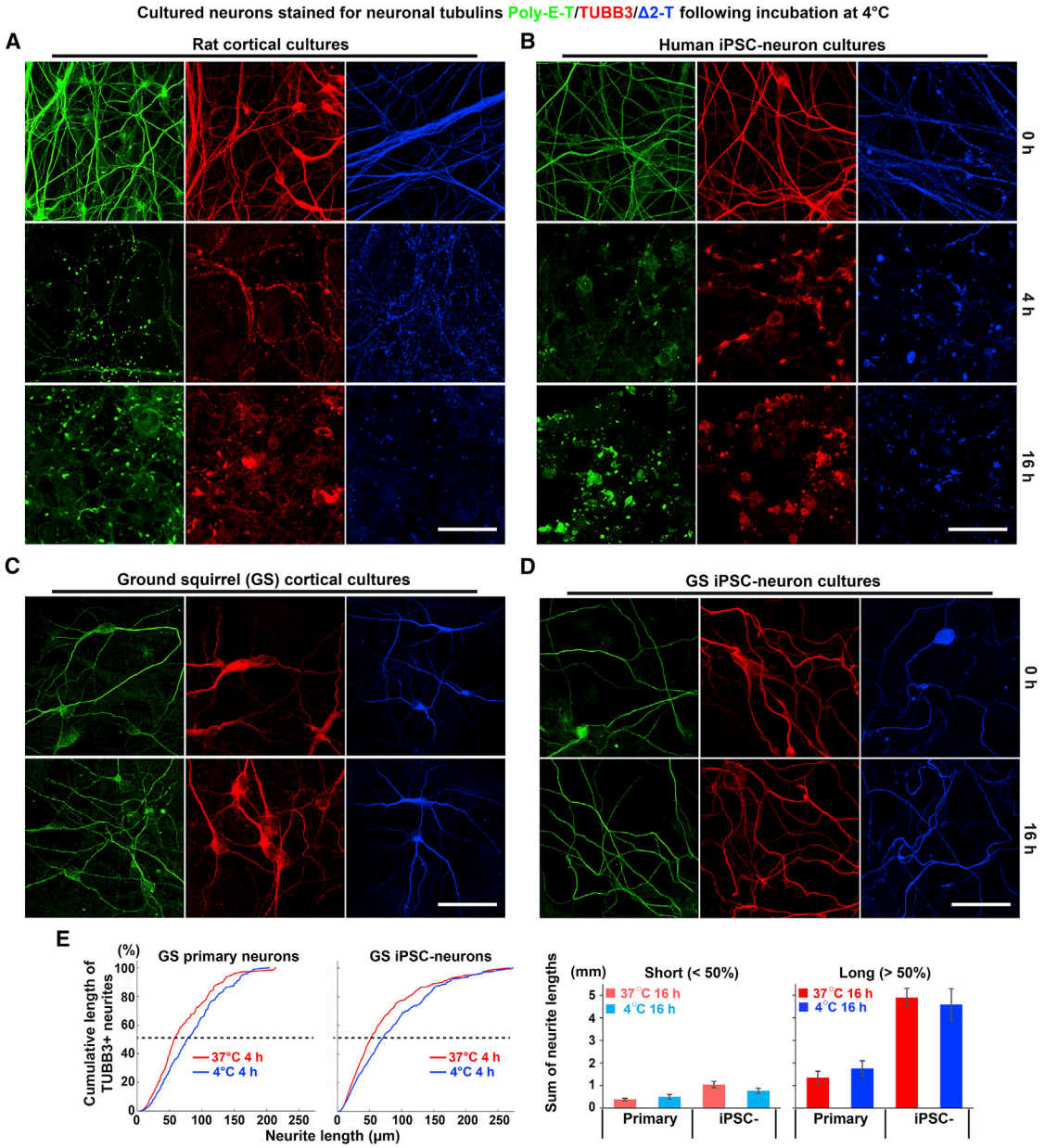


**Figure 1. Species-Dependent Differences in Neuronal Microtubule Cold Stability**

(A) Immunofluorescence of TUBB3 (red), polyglutamylated tubulin (poly-E-T, green), or delta2-tubulin (Δ2-T, blue) in cultured rat primary cortical neurons incubated at 4°C for various durations. Scale bar, 40 μm.

(B) Immunofluorescence of TUBB3, poly-E-T, or Δ2-T in cultured human induced pluripotent stem cell-derived neurons (iPSC-neurons) incubated at 4°C for various durations. Scale bar, 40 μm.

(C) Immunofluorescence of TUBB3, poly-E-T, or Δ2-T in cultured 13-lined ground squirrel (GS) primary cortical neurons incubated at 4°C for various durations. Scale bar, 40 μm.

(D) Immunofluorescence of TUBB3, poly-E-T, or Δ2-T in GS iPSC-neurons incubated at 4°C for various durations. Scale bar, 40 μm. For other cell types differentiated from GS iPSCs, see also Figure S1.

(E) Cumulative plots and quantification of the lengths of manually traced TUBB3-positive microtubules (see STAR Methods) from GS cortical primary neurons (n = 5 experiments each at 37°C and 4°C; cultures derived from 4 GS pups) and GS iPSC-neurons (n = 6 experiments each at 37°C and 4°C; cultures derived from 2 GS iPSC lines). Cumulative lengths of short (neurite lengths <50% of the cumulative plots) and long microtubules (neurite lengths >50% of the cumulative plots) were quantified separately. No significant difference in microtubule length attributed to cold temperature was found ($p > 0.05$; Student's t test for two-group comparison). Error bars indicate SEM.

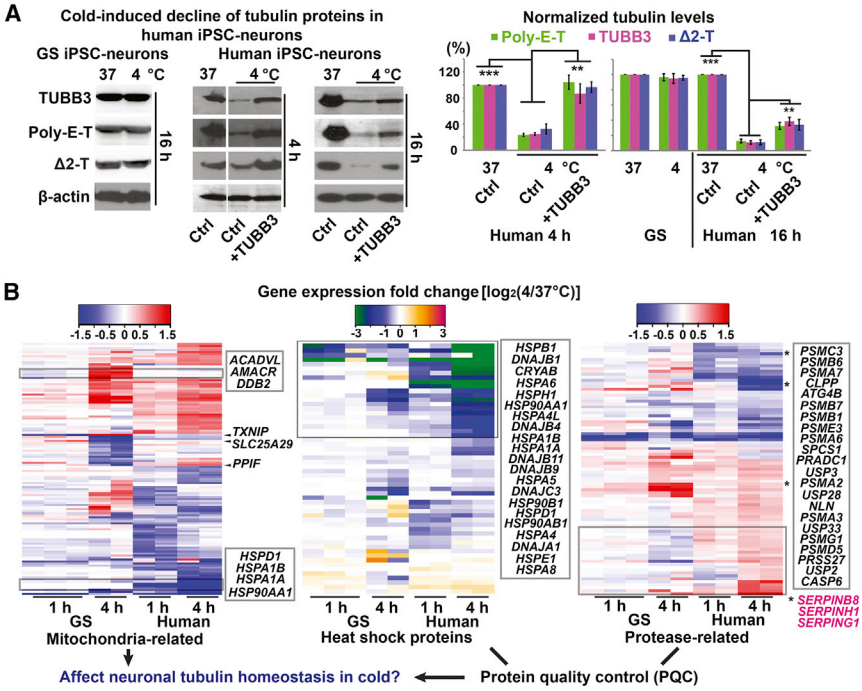


**Figure 2. Species-Dependent iPSC-Neuronal Transcriptome Changes in Mitochondria and Protein Quality Control in Response to Low Temperature**

(A) Western blots and quantification of TUBB3, poly-E-T, and Δ2-T proteins in GS and human iPSC-neurons following 4- or 16-hr cold exposure with or without TUBB3 overexpression (n = 5 experiments from 2 GS and 2 human cell lines; Student's t test between untreated controls with or without cold exposure and between cold-exposed groups with or without the *TUBB3* overexpression plasmid; **p < 0.01; ***p < 0.001). Error bars indicate SEM. See also Figure S2C.

(B) Heatmaps of transcriptomic alterations in GS and human iPSC-neuronal cultures induced by 4°C incubation for 1 hr or 4 hr (see STAR Methods), highlighting two distinct categories of expression: genes related to mitochondrial functions and genes encoding heat-shock proteins (HSPs), proteases, and proteinase inhibitors (*SERPINs*, magenta). Some genes exhibiting distinct alteration patterns between GS and human are emphasized. See also Figure S3 and Data S1–S3.

mitochondrial membrane potential ($\Delta\psi_m$) changes. In human iPSC-neurons following a temperature decrease from 37°C to 10°C, we observed a hyperpolarizing $\Delta\psi_m$ (Figure 3A; Movie S1). In contrast, when GS iPSC-neurons were treated with the same experimental protocol, we instead observed a depolarizing $\Delta\psi_m$ (Figure 3A). Although this change is seemingly minute, it leads to a significant increase in reactive oxygen species (ROS) production (see Discussion). Indeed, following 30-min cold exposure, we observed significantly higher cold-induced ROS production in human than in GS iPSC-neurons (Figure 3B), indicating that the immediate mitochondrial response results in prolonged oxidative stress. Importantly, when the human iPSC-neuron mitochondrial hyperpolarization was reversed by the addition of a low dose of mitochondrial uncoupler, BAM15 (0.1 μM, Figure 3A), we observed a significant decrease in ROS production, to a level comparable to GS iPSC-neurons in the cold (Figure 3B).

Because ROS may oxidize and disrupt microtubules (Wilson and González-Billault, 2015), we hypothesized that the GS iPSC-neurons possess superior microtubule stability due to suppressed ROS generation as a consequence of muted hyperpolarizing $\Delta\psi_m$ in response to cold. To verify this, we directly probed cold-induced protein oxidation. We found that levels of oxidized proteins increased in human iPSC-neurons but remained unchanged in GS iPSC-neurons exposed to cold for 16 hr (Figure 3C). Oxidized proteins are subject to protein-protein cross-linkages and aggregate formation (Gregersen and Bross, 2010; Grune et al., 1997). Indeed, immunolabeling of oxidized proteins revealed aggregates along residual microtubules after cold exposure in human but not in GS iPSC-neurons (Figures 3D and S4). Interestingly, the addition of BAM15 prevented accumulation of oxidized proteins along microtubules (Figure 3D). Thus, our findings suggest that overproduction of ROS via cold-induced mitochondrial hyperpolarization leads to microtubule damage and subsequent aggregation.

## Cold Causes Lysosomal Membrane Permeabilization in Human iPSC-neurons

Damaged proteins would normally engage the PQC system for their removal (Goldberg, 2003; Zhang and Ye, 2014), with lysosomes providing an alternative pathway to the ubiquitin-proteasome machinery (Dunlop et al., 2009; Iwata et al., 2005; Lee et al., 2012). However, in cold-exposed human iPSC-neurons, we observed a PQC dysregulation (Figures 2B, S5B, and S5C) and, surprisingly, evidence of compromised lysosomal integrity (i.e., lysosomal membrane permeability [LMP]), which acidifies the cytosol and releases digestive enzymes. To assess the latter, we loaded GS and human iPSC-neurons with Magic Red and DND-26, which labeled discrete puncta of lysosomal vesicles. However, in cold-exposed human neurons, more diffuse cytosolic Magic Red and DND-26 signals were observed (Figure 4A, arrowheads)—typical signs of LMP and an acidified cytosolic environment. Thus, proteases leaked from lysosomes are poised to inadvertently digest cytosolic proteins such as adjacent microtubules. Notably, BAM15 and the antioxidant vitamin C significantly reduced LMP (Figure 4B), demonstrating a link between cold-induced mitochondrial dysfunction and LMP.

## Cold-Exposed Human iPSC-Neuronal Microtubules Are Protected by Uncoupling Mitochondria and Neutralizing the Adverse Effect of LMP

Motivated by our bioinformatics and experimental results, we sought to determine whether pharmacological intervention

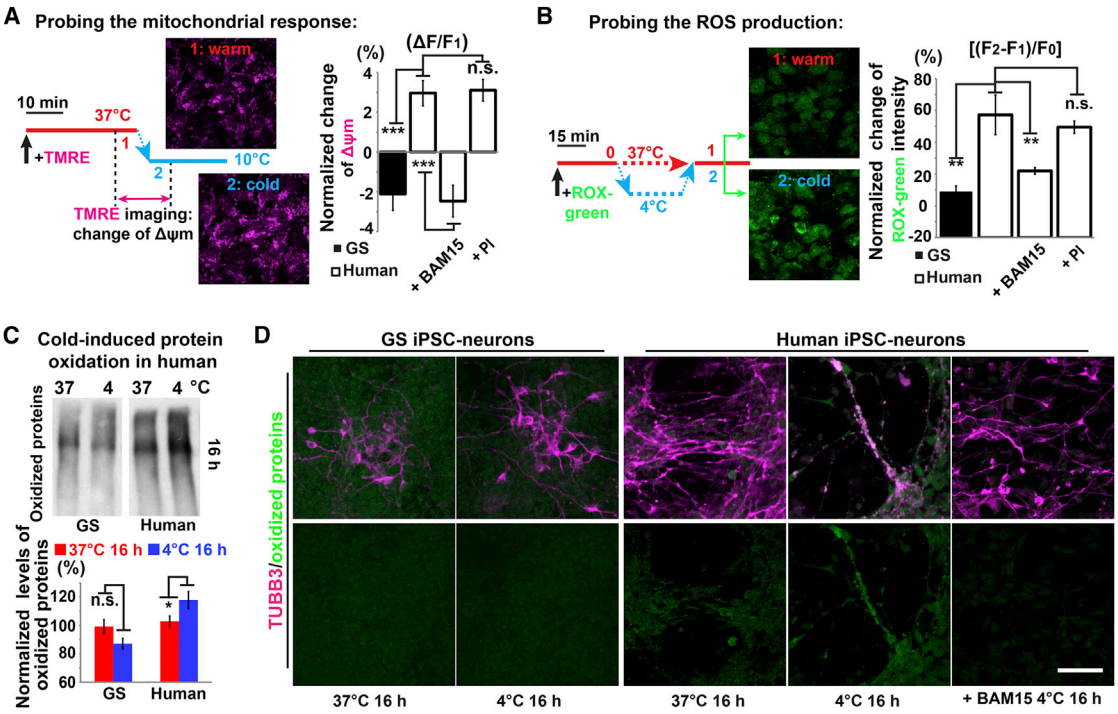


**Figure 3. Cold-Induced Mitochondrial Hyperpolarization and Oxidative Stress in Human iPSC-Neurons**

(A) Left: Live-cell-imaging protocol of mitochondrial membrane potential ($\Delta\psi_m$) with TMRE (see STAR Methods). Right: Quantification of cold-induced $\Delta\psi_m$ changes in GS and human iPSC-neurons untreated controls and treated with BAM15 or PI (n = 8 experiments; Student's t test between GS and human controls; ANOVA plus post hoc Tukey test for multiple human cold-exposed groups with or without drug treatment; ***$p < 0.001$; n.s. $p > 0.05$, not significant). BAM15, a mitochondrial uncoupling drug; PI, protease inhibitors. Error bars indicate SEM. See also Movie S1.

(B) Left: CellROX green imaging protocol to assess cold-induced ROS production (see STAR Methods). Right: Quantification of ROS production following 30-min cold exposure in GS and human iPSC-neurons (n = 8 experiments; Student's t test between GS and human comparisons; ANOVA plus post hoc Tukey test for multiple human cold-exposed groups with or without drug treatment; **$p < 0.01$; n.s. $p > 0.05$, not significant). Error bars indicate SEM.

(C) Western blots and quantification of oxidized proteins following 16-hr incubation at 4°C (n = 5 experiments; Student's t test for two-group comparisons; *$p < 0.05$). Error bars indicate SEM.

(D) Immunofluorescence of TUBB3 (magenta) and oxidized proteins (green). Note: After 16-hr incubation at 4°C, minimal protein oxidation was detected on GS TUBB3+ processes even with digital enhancement, while in human neurons oxidized proteins were found on residual TUBB3+ microtubules, which could be reduced or completely mitigated by BAM15 treatment (n = 5 experiments). Scale bar, 50 μm. See also Figure S4. For all experiments in this figure, neurons were derived from 2 GS and 3 human iPSC lines for each group.

targeting the affected pathways could confer the GS's microtubule cold resistance upon non-hibernating mammals. Indeed, a low dose of BAM15 preserved long neurites and tubulin proteins in human iPSC-neurons incubated at 4°C for 4 hr (Figures 5A–5C). Reinforcing the notion that this protection arises directly from the uncoupling effect of BAM15, transient overexpression of mitochondrial uncoupler proteins UCP1 or UCP2 (Laursen et al., 2015; Yamashita et al., 1999) in human iPSC-neurons likewise produced cold-stable neurites (Figures S6A, S6B, and S6E).

Additionally, we pretreated human iPSC-neurons with a protease inhibitor cocktail (PI) to alleviate the adverse effects of leaked proteases from LMP. PI effectively preserved long neurites in cold-exposed human iPSC-neurons (Figures 5A–5C). Notably, PI did not alter $\Delta\psi_m$ hyperpolarization or ROS production (Figures 3A and 3B), suggesting that LMP induction lies downstream of mitochondrial activities. Remarkably, the combination of BAM15 and PI further preserved human iPSC-neuron microtubules to near-control levels (Figure 5B), suggesting that—in addition to triggering LMP—ROS may directly damage microtubules as demonstrated in Figures 3D and S4. A working model is demonstrated in Figure 5D.

## BAM15 and Protease Inhibitors Preserve Morphology and Function in the Rat Retina during Cold Stress

Promising results from our *in vitro* experiments prompted us to test whether these treatments can also protect neural tissues of a non-hibernator when challenged with hibernation-like hypothermia. We used an *ex vivo* rat retina preparation, which retains intact neural structure and responds to light under healthy conditions.

Like human iPSC-neurons, cold-exposed retinal ganglion cells (RGCs) in rat retina exhibited considerable microtubule destruction, losing most of their dendritic microtubules and forming numerous tubulin aggregates along their axons (Figures 6A and 6B). In contrast, retinal tissues from hibernating GS showed no changes in microtubule morphology (data not shown). Strikingly, pre-incubation of rat retinas with BAM15 and PI greatly

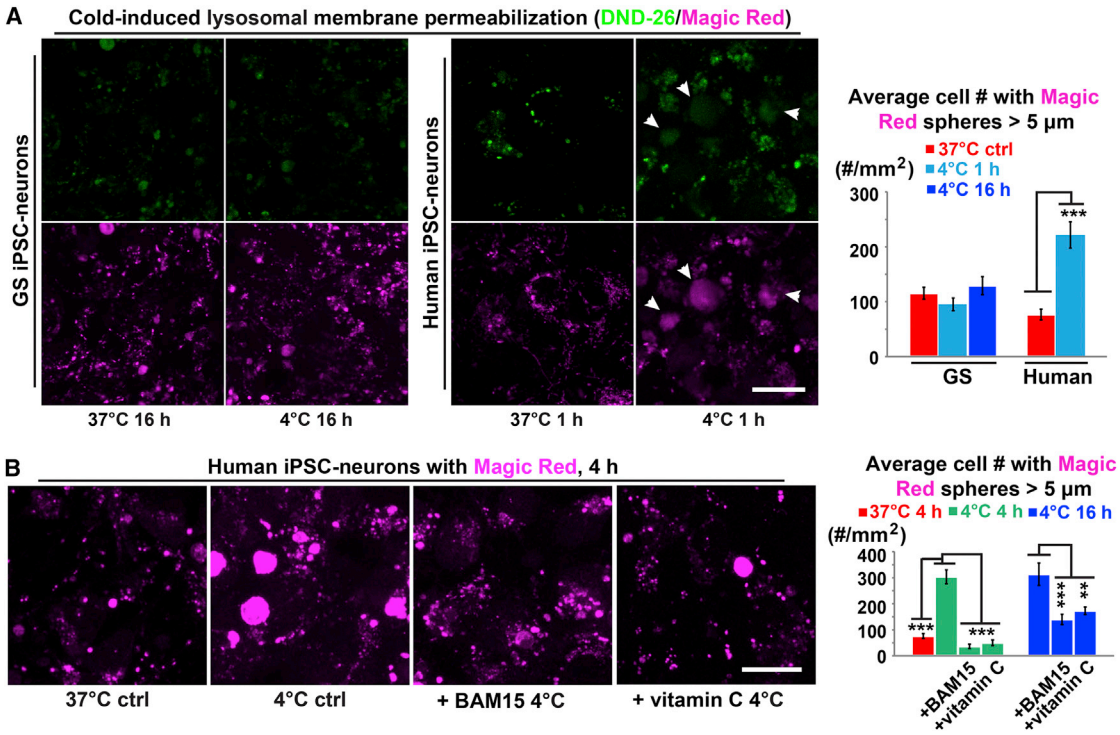


**Figure 4. Cold-Induced Lysosomal Membrane Permeabilization in Human iPSC-Neurons**

(A) Left: Live imaging of lysosomes in GS and human iPSC-neurons with DND-26 (green) and Magic Red (magenta; see STAR Methods). Note: Following 1-hr incubation at 4°C, accumulation of diffuse cytoplasmic fluorescence in marked human neurons (arrowheads) indicating LMP. Scale bar, 20 μm. Right: Quantification of cells containing diffused Magic Red signals (diameter > 5 μm) (n = 6 experiments; Student's t test for two-group comparison; ***$p < 0.001$). Error bars indicate SEM.

(B) Left: Live imaging of lysosomes in human iPSC-neurons with Magic Red under denoted conditions. Note: BAM15 (0.1 μM) or the antioxidant vitamin C (0.5 mM) alleviated LMP in human neurons treated following 4-hr incubation at 4°C. Scale bar, 20 μm. Right: Quantification of cells containing diffused Magic Red signals (diameter > 5 μm) (n = 5 experiments; Student's t test between untreated controls with or without cold exposure; ANOVA plus post hoc Tukey test for multiple cold-exposed groups; **$p < 0.01$; ***$p < 0.001$). See also Figure S5 for the involvement of other PQC components. For these experiments, neurons were derived from 2 GS and 3 human iPSC lines for each group. Error bars indicate SEM.

reduced the RGC microtubule defects caused by cold-exposure (Figures 6A and 6B).

We then used multi-electrode array (MEA) recordings to measure RGC activity. As shown in Figure 6C, incubation at 4°C for 4 hr largely silenced rat RGCs and greatly reduced the average firing rates of remaining RGCs, whereas pre-treatment with BAM15 and/or PI significantly preserved rat RGC activity (Movie S2). In contrast, 10 μM Taxol (a classic microtubule stabilization drug) did not preserve RGC activity in cold-exposed rat retinas (Figure 6C), even though it preserved long neurites (Figure S2D). Further, we assessed the RGC light response, which is a strong indicator of the health and proper function of the retina (Figure 6D; Movie S3). In control rat retinas, approximately 70% of the RGCs sorted based on their spontaneous activities were light responsive, compared to only 5% in untreated rat retinas after 4°C for 4 hr. However, RGCs in cold-incubated rat retinas pre-treated with BAM15 or PI, but not Taxol, displayed 7- to 11-fold increases in light responsiveness. Taken together, these results indicate that uncoupling mitochondria and/or inhibiting lysosomal protease activity substantially enhanced cold-tolerance in cultured neurons and supported functional recovery of neural tissues from non-hibernating mammals.

## BAM15 and Protease Inhibitors Improve Mouse Kidney Protection during Cold Storage and Rewarming

We further tested whether the microtubule protective effect of BAM15/PI treatment can be extended to non-neural tissues, specifically to organs awaiting transplantation, which are commonly cold stored and re-warmed in conditions comparable to GS hibernation (McAnulty, 2010; Mitchell et al., 2011) (Figure S1E). As reported previously (Breton and Brown, 1998; Mangino et al., 2008), we found that mouse kidneys stored in University of Wisconsin (UW) solution at 4°C for 24 hr exhibited microtubule damage with drastically reduced tubulin labeling (especially in glomeruli), with limited recovery after re-warming (Figure 7). Remarkably, adding BAM15 and PI to the UW solution significantly improved tubulin signals in the cold and bestowed prominent recovery of microtubule morphology after re-warming (Figure 7). In addition, BAM15 and PI also greatly reduced known adverse effects of extended cold storage to the kidney, such as protein/DNA damage

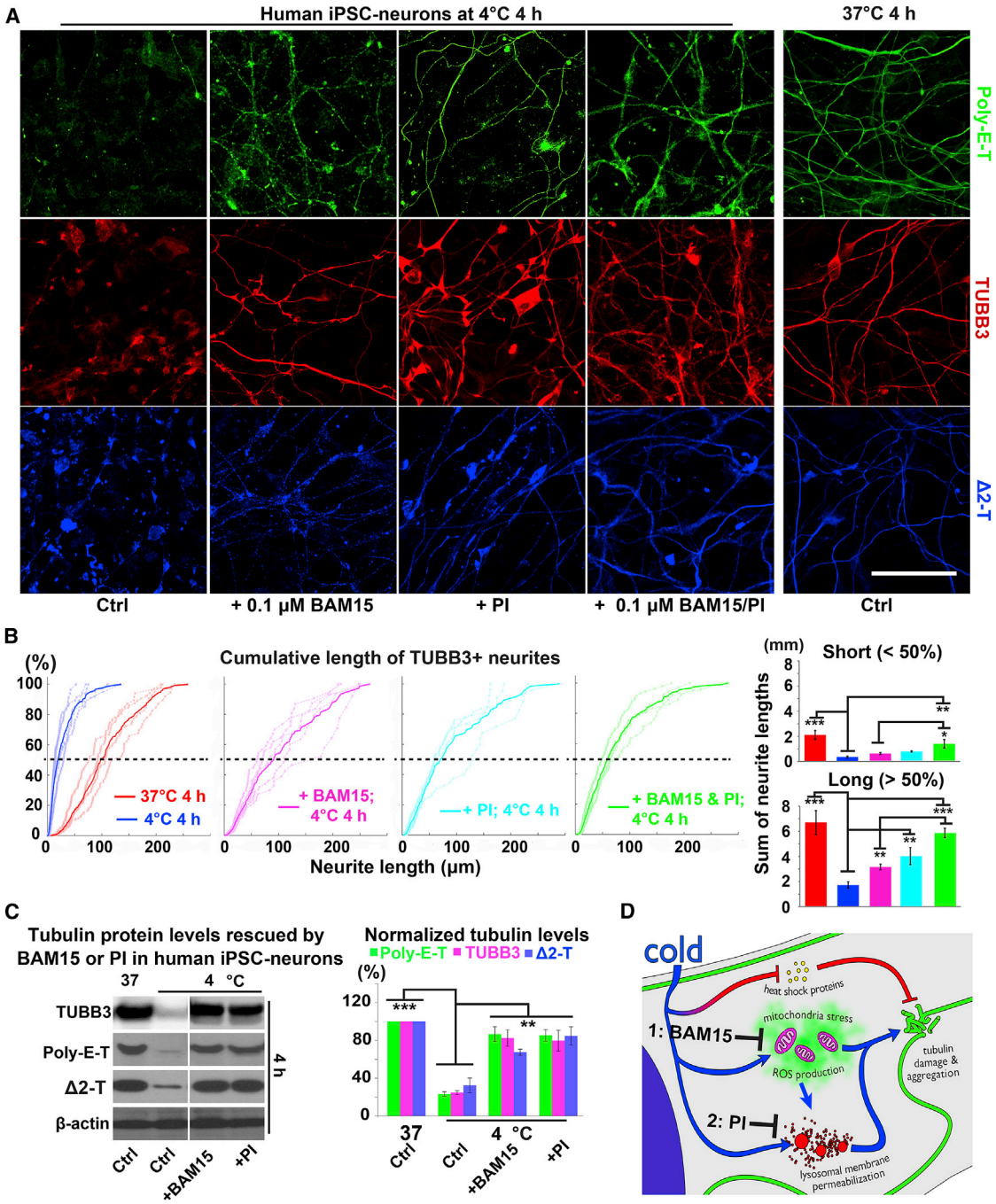


**Figure 5. Morphological Protection of Human iPSC-Neurons by BAM15/PI Pretreatments against Prolonged Cold Stress**

(A) Pretreatment with BAM15 (0.1 μM; n = 17 experiments), PI (1:500; n = 24 experiments), or a combination of both (n = 20 experiments) preserved long neurites (poly-E-T, green; TUBB3, red; Δ2-T, blue) of human iPSC-neurons following 4-hr incubation at 4°C. Scale bar, 40 μm. See also Figure S6.

(B) Cumulative plots and quantification of TUBB3+ neurite lengths (see STAR Methods; BAM15, n = 6 experiments; PI, n = 5 experiments; BAM15 and PI, n = 6 experiments; Student's t test between untreated controls with or without cold exposure; ANOVA plus post hoc Tukey test for multiple cold-exposed groups treated for the same duration; *p < 0.05; **p < 0.01; ***p < 0.001). Error bars indicate SEM.

(C) Western blots and quantification confirming that BAM15 or PI pretreatment maintained tubulin protein levels in human iPSC-neurons after 4-hr incubation at 4°C (n = 5 experiments; Student's t test between untreated controls with or without cold exposure; ANOVA plus post hoc Tukey test for multiple cold-exposed groups; **p < 0.01; ***p < 0.001). Error bars indicate SEM.

(D) Proposed model depicting the mechanisms by which BAM15 and PI pretreatments protect human iPSC-neurons from cold stress. For these experiments, human neurons were derived from 3 iPSC lines.

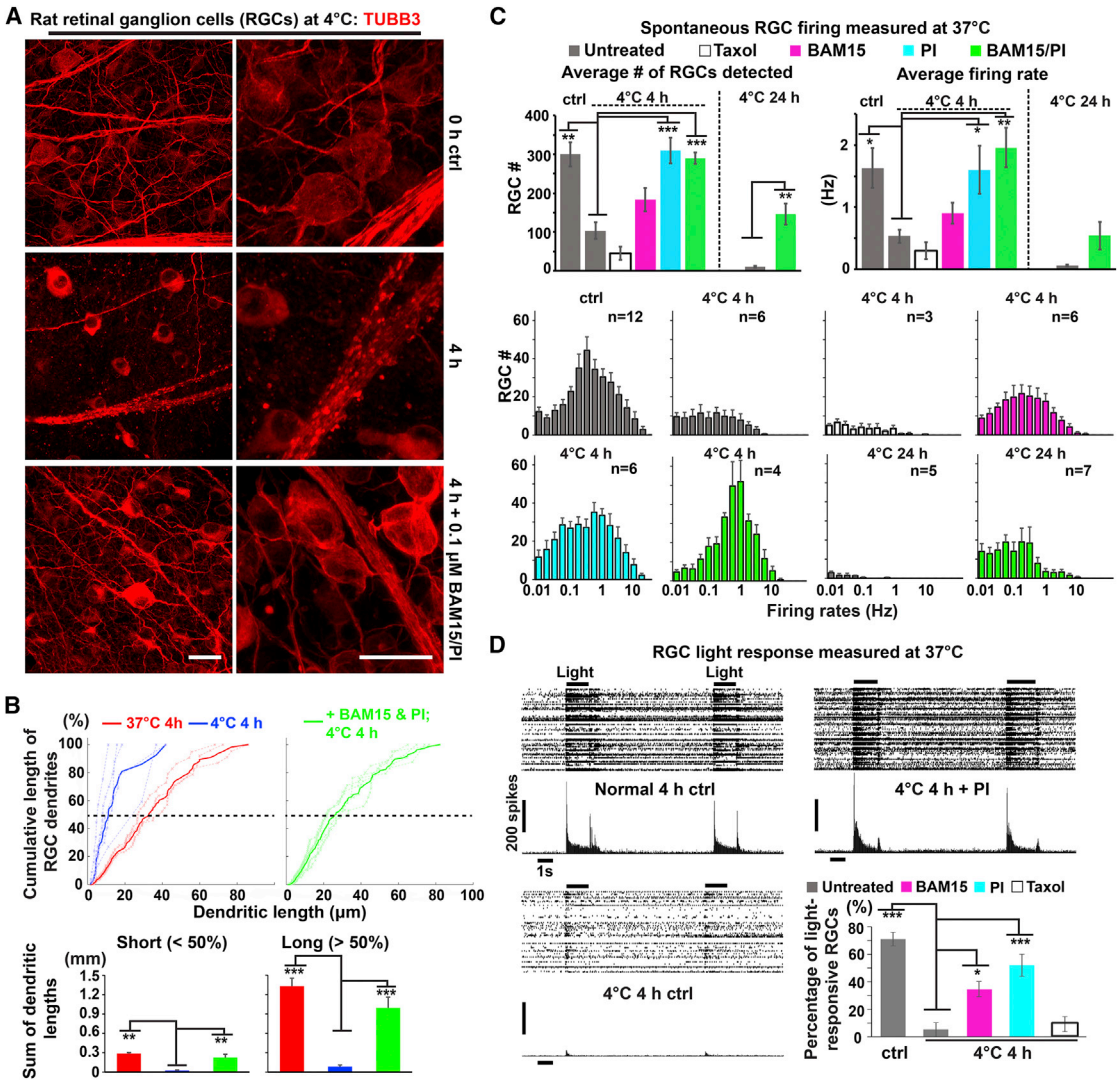


**Figure 6. Morphological and Functional Protection of Rat Retinal Explants by BAM15/PI Pretreatments against Prolonged Cold Stress**

(A) Microtubule morphology in rat (n = 10 animals) retinal ganglion cells (RGCs) immunostained for TUBB3 (red). Scale bars, 20 μm.

(B) Cumulative plots and quantification of TUBB3+ RGC dendritic lengths in rat retina (see STAR Methods; n = 6 animals; Student's t test for two-group comparisons; **p < 0.01; ***p < 0.001). Error bars indicate SEM.

(C) Quantification of multielectrode array (MEA) recordings of spontaneous RGC activity following exposure to 4°C for 0 hr, 4 hr, or 24 hr. Treatments and their corresponding color legend are indicated. Upper Left: Numbers of active RGCs detected by MEA. Upper Right: Average firing rates for detected RGCs. Lower: Distributions of firing rates for detected RGCs. Student's t test between untreated controls with or without cold exposure and the 24-hr cold-exposed groups; ANOVA plus post hoc Tukey test for multiple cold-exposed groups treated for the same duration; *p < 0.05; **p < 0.01; ***p < 0.001. Error bars indicate SEM. See also Movie S2 for an animated example of MEA recordings of the RGC spontaneous firing. The number of animals used in each condition is provided in the histogram.

(D) Representative light responses of rat RGCs following 4-hr cold exposure either untreated or treated with BAM15 (n = 5 animals), PI (n = 6 animals), or Taxol (n = 6 animals). Quantification is provided as the percentage of detected RGCs that were light responsive (see STAR Methods; Student's t test between untreated controls with or without cold exposure; ANOVA plus post hoc Tukey test for multiple groups cold-exposed for the same duration; *p < 0.05; ***p < 0.001). Error bars indicate SEM. See also Movie S3 for an animated example of MEA recordings of the light response experiments.

caused by lipid peroxidation (Cotterill et al., 1989) and cell apoptosis (Jain et al., 2016) (Figures S7A and S7B). These results indicate that similar cellular mechanisms lead to cold-induced microtubule instability in various tissues and organs in non-hibernators. Thus, BAM15/PI treatment may also confer cold protection to non-neural tissues and organs and prolong their shelf-life for transplantation.

## DISCUSSION

### GS iPSCs Are a Versatile Platform to Study Tissue/Cell-Type-Specific Cold Adaptive Features of Hibernating Mammals

Hibernating animals display various tissue-specific, cold-adaptive features, each an incredible biological marvel waiting to be

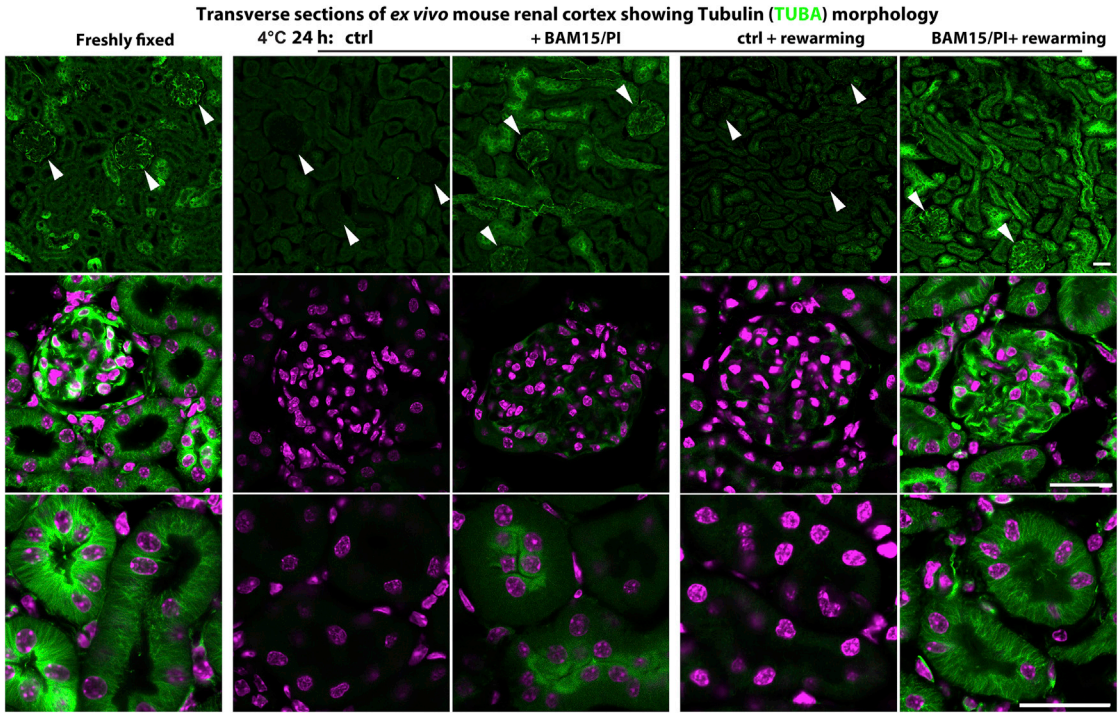


**Figure 7. Protecting Mouse Kidneys with BAM15/PI during Cold Storage**

Immunofluorescence of α-tubulins (TUBA, green) and DAPI (magenta) in transverse sections of wild-type mouse kidneys under these conditions (n = 4–6 animals used for each condition): freshly fixed, after 24-hr cold storage at 4°C (with or without BAM15/PI), or rewarming at 37°C (with or without BAM15/PI) for 30 min following 24-hr cold storage. Note: Reduced tubulin signals in glomeruli (arrowheads in upper, middle) and renal tubular epithelium (lower) of mouse kidneys stored at 4°C for 24 hr in standard University of Wisconsin (UW) solution. Scale bars, 25 μm in all panels. See also Figure S7 for oxidative damages and cell apoptosis in mouse kidneys during cold storage.

understood (Staples, 2016). To empower effective *in vitro* study of these hibernation features in diverse cell and tissue types, we generated iPSCs from the GS. Most importantly, we demonstrated that cells derived from GS iPSCs retained native cold-resistant features and discovered a link between cold-induced mitochondrial stress, PQC dysfunction (e.g., LMP), and microtubule instability—problems that are apparently solved in hibernators. Inspired by this finding, we sought to alleviate these problems in non-hibernator cells and tissues by reducing ROS production, LMP, and protein degradation. These manipulations protected the microtubule integrity of human iPSC-neurons and preserved retinal functions in rat retina explants that were otherwise eradicated at near-freezing temperatures. Furthermore, the same treatments also protected mouse kidneys from microtubule and other cellular damage in conditions mimicking cold storage for transplantation.

Cooling and therapeutic hypothermia (mild hypothermia) have been shown to be neuroprotective (Delhaye et al., 2012; Peretti et al., 2015; Yenari and Han, 2012), in which upregulation of cold-shock proteins such as RBM3 appears to be essential (Bastide et al., 2017; Tong et al., 2013; Zhu et al., 2016). We observed a similar surge of RBM3 proteins in human and GS iPSC-neurons exposed to 33°C for 60 hr, but not at hibernation-like temperatures (<10°C) (Figure S2B), consistent with previous reports (Tong et al., 2013; Zhu et al., 2016). These findings suggest that mild hypothermia and hibernation-like hypothermia may involve distinct sets of molecular mediators or may reflect different translational regulations under these two conditions (Bastide et al., 2017; Qiang et al., 2013). While mice with various genetic manipulations can serve as powerful models for studying mild hypothermia (Peretti et al., 2015), the GS iPSC lines reported here provide a valuable alternative for investigating hibernation-like hypothermia.

Although iPSCs may not recapitulate all *in vivo* cellular features due to possible epigenetic changes during the reprogramming process (Mertens et al., 2015), many intrinsic cellular features are preserved, facilitating *in vitro* disease modeling and drug screening (Avior et al., 2016). As an example, microtubule cold-stability is retained in GS iPSC-neurons.

## Microtubules Can Be Protected by Multiple Levels of Regulation during Cold Exposure

Potential mechanisms for microtubule cold stability in GS iPSC-neurons include the following: (1) Different isotypes or amino acid sequences of tubulins may confer cold-resistance as in Antarctic fish (Detrich and Parker, 1993). However, we found that the predicted protein sequences of the major tubulin types in GS are over 99% identical to those of human, mouse, or rat (data not shown). (2) Tubulins may undergo post-translational modifications (PTMs), which can alter microtubule stability (Hammond et al., 2008; Song et al., 2013). For example, a thorough proteomic study from GS revealed that low body

temperature alters the PTMs of cytoskeletal regulatory proteins (Hindle and Martin, 2013), and PTMs have been implicated in metabolic and proteostatic regulation in hibernating bat brain (Zhang et al., 2014). However, we did not find significantly different expression patterns of common neuron-enriched PTMs, such as poly-E-T and Δ2-T, in human and GS iPSC-neurons (Figures 1 and 2A); similar expression patterns were likewise found for tyrosinated or acetylated tubulins (data not shown). (3) MAPs have also been shown to stabilize microtubules (Billger et al., 1991). For example, in hibernating GS, hyper-phosphorylation of tau may play a role in stabilizing neuronal microtubules (Arendt and Bullmann, 2013). Neuronal microtubules are stabilized by MAP6 to withstand short-term cold exposure (~4°C for 30–60 min) (Bosc et al., 2003; Guillaud et al., 1998). We found MAP6 was present but not differentially regulated by temperature in either human or GS iPSC-neurons (Data S3). Nonetheless, these established mechanisms are apparently insufficient to bestow non-hibernating mammals with microtubule stability in hibernation-like hypothermia for prolonged periods of time (Figures 1 and 6; see also Taylor, 2006). Accordingly, here we have identified mitochondria-lysosome pathways as yet another level of regulation for microtubule stability.

## Prevention of Cold-Induced ROS Overproduction Stabilizes Microtubules

We observed that cold exposure induced $\Delta\psi_m$ hyperpolarization and ROS overproduction in human iPSC-neurons, whereas mitochondria in cold-exposed GS iPSC-neurons depolarized and produced significantly less ROS. Consistent with our findings, mild hypothermia has been reported to hyperpolarize isolated mouse mitochondria and increase ROS production (Ali et al., 2010). Owing to a steep nonlinear relationship between $\Delta\psi_m$ and ROS production for mitochondria near the normal ranges of $\Delta\psi_m$ (Starkov and Fiskum, 2003), the seemingly modest changes in $\Delta\psi_m$ observed here in fact correspond to substantial changes in ROS production, as demonstrated by direct ROS measurements (Figure 3B). Mitochondrial ROS generation is the major source of oxidative damage to proteins and membranes (Balaban et al., 2005) and likely contributes to the microtubule destruction observed in cold-exposed human iPSC-neurons and rat neural tissues. Hibernators, on the other hand, may have evolved strategies that evade oxidative stress by minimizing mitochondrial hyperpolarization. Consistent with this notion, in winter, the maximum $\Delta\psi_m$ of GS brain mitochondria during torpor (5°C) is slightly more depolarized compared to that during interbout arousals (37°C) (Ballinger et al., 2017). Intriguingly, in both states, $\Delta\psi_m$ is more hyperpolarized than in spring, suggesting possible seasonal pre-conditioning. Mechanistically, either free fatty acids (Dedukhova et al., 1991; Skulachev, 1991), produced by augmented lipid metabolism during hibernation, or intrinsic uncoupling protein expression (Andrews et al., 2005; Boyer et al., 1998; Laursen et al., 2015; Liu et al., 2006) could result in higher proton leak, thus conferring protection against cold-induced ROS damage. Consistently, transient overexpression of UCP1/UCP2 in human iPSC-neurons enhanced microtubule cold stability.

## Cold-Induced PQC Dysfunction Destabilizes Microtubules

In line with RNA sequencing (RNA-seq) data, our experimental results indicate that protein degradation pathways are compromised by cold exposure. Impairment of HSP/proteasome pathways may redirect protein degradation to the autophagosome/lysosome pathway (Dunlop et al., 2009; Iwata et al., 2005; Lee et al., 2012). However, protein levels of key autophagosome-lysosomal components did not change significantly in cold-exposed human iPSC-neurons (Figure S5D).

Instead, detrimental interactions may result from the juxtaposition of lysosomes and microtubules (Figure S5E) in cold-exposed human iPSC-neurons. Lysosomal dysfunction has been reported to impair microtubule structure (Fukuda et al., 2006). In turn, both destabilized microtubules and oxidative stress have been shown to lead to LMP (Boya and Kroemer, 2008; Roberg and Ollinger, 1998). Taken together, impaired PQC components coupled with ROS overproduction by stressed mitochondria may form a vicious cycle, resulting in irreversible protein damage and aggregation in the cold. Remarkably, we discovered that GS iPSC-neurons are free from all these adverse cellular responses to cold. A potential mechanism of PQC cold adaptation may be attributed to enhanced organelle membrane integrity in GS cells due to their unique lipid redistribution (Azzam et al., 2000) and may be explored further using the GS iPSC-model.

## Pharmacological Interventions May Confer Cold Resistance upon Human Tissues for Clinical Applications

Our findings on microtubule cold stability have compelling clinical applications, such as prolonging the survival of organs awaiting transplantation (Maathuis et al., 2007; Niemann et al., 2015). Prolonged cold storage has been shown to induce mild oxidative stress to organs (Fabre et al., 2002). Therefore, the standard cold-storage medium, UW solution, is enriched in antioxidant components. Nonetheless, even with UW solution (Mangino et al., 2008) or other physiological solutions (Breton and Brown, 1998), cold-induced disruption and degradation of microtubules still occur. Here, we show that the addition of BAM15/PI to UW solution greatly enhanced tubulin preservation in the cold and promoted repolymerization upon rewarming—possibly by alleviating mitochondrial stress and hence reducing ROS production and tubulin damage caused by LMP.

This tissue-protective strategy is likely applicable to other transplantable organs. In addition, it demonstrates that, by understanding the biology of cold adaptation in hibernation, we can improve and broaden the applications of hypothermia, which has the benefit of metabolic suppression but is often hampered by cold-induced cellular damage (Marion et al., 1997). With the pluripotency of GS iPSCs, unique cold-resistant features of different tissues can be explored more easily *in vitro*. Furthermore, extreme temperature is only one form of stressor to which the hibernator is adapted. We propose that GS iPSCs can be used to elucidate cellular mechanisms of adaptation to other insults such as metabolic stress, hypoxia/reperfusion injury, and inflammatory damage, potentially allowing us to harness protective effects for therapeutic uses.

## STAR★METHODS

Detailed methods are provided in the online version of this paper and include the following:

- KEY RESOURCES TABLE
- CONTACT FOR REAGENT AND RESOURCE SHARING
- EXPERIMENTAL MODEL AND SUBJECT DETAILS
  - Animals
  - Primary Cultures
- METHOD DETAILS
  - Reprogramming of neonatal GS NPCs into iPSC colonies
  - Validation of GS iPSCs
  - Neuronal differentiation of human and GS iPSCs, and rat cortical primary cultures
  - Evaluation of microtubule cold-stability
  - Multielectrode array (MEA) measurements
  - Western blotting and immunostaining
  - RNA-sequencing
  - Mapping, quantification and differential expression analysis of RNA-seq data
  - Functional enrichment analysis of altered transcripts
  - Tubulin protein sequence homology analysis
  - Acetylation prediction analysis of tubulin proteins
  - Live cell imaging of mitochondrial membrane potential (TMRE)
  - Live cell imaging of ROS production (CellROX-green)
  - Live cell imaging of lysosomes using Magic Red and DND-26
  - Neurite tracing
  - Detection of protein aggregates
  - Evaluation on mouse kidneys after cold storage
- QUANTIFICATION AND STATISTICAL ANALYSIS
- DATA AND SOFTWARE AVAILABILITY

## SUPPLEMENTAL INFORMATION

Supplemental Information includes seven figures, one table, three movies, and three data files and can be found with this article online at https://doi.org/10.1016/j.cell.2018.03.010.

A video abstract is available at https://doi.org/10.1016/j.cell.2018.03.010#mmc8.

## ACKNOWLEDGMENTS

We thank Drs. Robert Balaban, Jeffrey Diamond, Tiansen Li, Antonina Roll-Mecak, Rosa Puertollano, Zuhang Sheng, Yihong Ye, Peter Yuen, and the members of the Li lab for critical discussions. Special thanks to Dr. Bing Zhou for his generous help and advice. Funding is provided by the Intramural Research Programs of the National Eye Institute ZIAEY000488-10 (W.L.), Joint Research Fund for Overseas Natural Science of China #31528012 (Z.X. and W.L.), National Institute of Neurological Disorders and Stroke ZICNS003008-14 (B.S.M.), and Center for Human Immunology, Autoimmunity and Inflammation (J.C. and H.Z.).

## AUTHOR CONTRIBUTIONS

Conceptualization, J.O. and W.L.; Methodology, J.O., Y.L., K.J.M., D.K.M., B.S.M., Z.X., and W.L.; Validation, J.O., J.M.B., T.Z., and Y.X.; Formal Analysis, J.O., J.M.B., Y.L. H.Z., J.C., and Z.X.; Investigation, J.O., J.M.B., T.Z., Y.X., H.Z., and J.C.; Resources, J.O, D.K.M., B.S.M., and W.L.; Data Curation, J.M.B., Y.L., J.C., Z.X., and W.L.; Writing, J.O., J.M.B., K.J.M., and W.L.; Visualization, J.O., J.M.B., and W.L.; Supervision, Z.X., B.S.M., and W.L.

## DECLARATION OF INTERESTS

The authors declare no competing financial interests. A provisional patent for the composition and methods to protect mammalian tissue against cold and other metabolic stresses has been filed by the NEI under US Application Serial No. 62/547,945.

Received: August 29, 2017
Revised: December 12, 2017
Accepted: March 2, 2018
Published: March 22, 2018

## REFERENCES

Ali, S.S., Marcondes, M.-C.G., Bajova, H., Dugan, L.L., and Conti, B. (2010). Metabolic depression and increased reactive oxygen species production by isolated mitochondria at moderately lower temperatures. J. Biol. Chem. *285*, 32522–32528.

Andrews, M.T. (2007). Advances in molecular biology of hibernation in mammals. BioEssays *29*, 431–440.

Andrews, Z.B., Diano, S., and Horvath, T.L. (2005). Mitochondrial uncoupling proteins in the CNS: in support of function and survival. Nat. Rev. Neurosci. *6*, 829–840.

Arendt, T., and Bullmann, T. (2013). Neuronal plasticity in hibernation and the proposed role of the microtubule-associated protein tau as a "master switch" regulating synaptic gain in neuronal networks. Am. J. Physiol. Regul. Integr. Comp. Physiol. *305*, R478–R489.

Arendt, T., Stieler, J., Strijkstra, A.M., Hut, R.A., Rüdiger, J., Van der Zee, E.A., Harkany, T., Holzer, M., and Härtig, W. (2003). Reversible paired helical filament-like phosphorylation of tau is an adaptive process associated with neuronal plasticity in hibernating animals. J. Neurosci. *23*, 6972–6981.

Avior, Y., Sagi, I., and Benvenisty, N. (2016). Pluripotent stem cells in disease modelling and drug discovery. Nat. Rev. Mol. Cell Biol. *17*, 170–182.

Azzam, N.A., Hallenbeck, J.M., and Kachar, B. (2000). Membrane changes during hibernation. Nature *407*, 317–318.

Balaban, R.S., Nemoto, S., and Finkel, T. (2005). Mitochondria, oxidants, and aging. Cell *120*, 483–495.

Ballinger, M.A., Schwartz, C., and Andrews, M.T. (2017). Enhanced oxidative capacity of ground squirrel brain mitochondria during hibernation. Am. J. Physiol. Regul. Integr. Comp. Physiol. *312*, R301–R310.

Barnes, B.M. (1989). Freeze avoidance in a mammal: body temperatures below 0 degree C in an Arctic hibernator. Science *244*, 1593–1595.

Bastide, A., Peretti, D., Knight, J.R., Grosso, S., Spriggs, R.V., Pichon, X., Sbarrato, T., Roobol, A., Roobol, J., Vito, D., et al. (2017). RTN3 is a novel cold-induced protein and mediates neuroprotective effects of RBM3. Curr. Biol. *27*, 638–650.

Billger, M., Strömberg, E., and Wallin, M. (1991). Microtubule-associated proteins-dependent colchicine stability of acetylated cold-labile brain microtubules from the Atlantic cod, *Gadus morhua*. J. Cell Biol. *113*, 331–338.

Bosc, C., Andrieux, A., and Job, D. (2003). STOP proteins. Biochemistry *42*, 12125–12132.

Boya, P., and Kroemer, G. (2008). Lysosomal membrane permeabilization in cell death. Oncogene *27*, 6434–6451.

Boyer, B.B., Barnes, B.M., Lowell, B.B., and Grujic, D. (1998). Differential regulation of uncoupling protein gene homologues in multiple tissues of hibernating ground squirrels. Am. J. Physiol. *275*, R1232–R1238.

Breton, S., and Brown, D. (1998). Cold-induced microtubule disruption and relocalization of membrane proteins in kidney epithelial cells. J. Am. Soc. Nephrol. *9*, 155–166.

Carey, H.V., Andrews, M.T., and Martin, S.L. (2003). Mammalian hibernation: cellular and molecular responses to depressed metabolism and low temperature. Physiol. Rev. *83*, 1153–1181.

Conde, C., and Cáceres, A. (2009). Microtubule assembly, organization and dynamics in axons and dendrites. Nat. Rev. Neurosci. *10*, 319–332.

Cooper, S.T., Richters, K.E., Melin, T.E., Liu, Z.J., Hordyk, P.J., Benrud, R.R., Geiser, L.R., Cash, S.E., Simon Shelley, C., Howard, D.R., et al. (2012). The hibernating 13-lined ground squirrel as a model organism for potential cold storage of platelets. Am. J. Physiol. Regul. Integr. Comp. Physiol. *302*, R1202–R1208.

Cotterill, L.A., Gower, J.D., Fuller, B.J., and Green, C.J. (1989). Oxidative damage to kidney membranes during cold ischemia. Evidence of a role for calcium. Transplantation *48*, 745–751.

Dave, K.R., Christian, S.L., Perez-Pinzon, M.A., and Drew, K.L. (2012). Neuroprotection: lessons from hibernators. Comp. Biochem. Physiol. B Biochem. Mol. Biol. *162*, 1–9.

Dedukhova, V.I., Mokhova, E.N., Skulachev, V.P., Starkov, A.A., Arrigoni-Martelli, E., and Bobyleva, V.A. (1991). Uncoupling effect of fatty acids on heart muscle mitochondria and submitochondrial particles. FEBS Lett. *295*, 51–54.

Delhaye, C., Mahmoudi, M., and Waksman, R. (2012). Hypothermia therapy: neurological and cardiac benefits. J. Am. Coll. Cardiol. *59*, 197–210.

Detrich, H.W., 3rd, and Parker, S.K. (1993). Divergent neural beta tubulin from the Antarctic fish Notothenia coriiceps neglecta: potential sequence contributions to cold adaptation of microtubule assembly. Cell Motil. Cytoskeleton *24*, 156–166.

Drew, K.L., Buck, C.L., Barnes, B.M., Christian, S.L., Rasley, B.T., and Harris, M.B. (2007). Central nervous system regulation of mammalian hibernation: implications for metabolic suppression and ischemia tolerance. J. Neurochem. *102*, 1713–1726.

Drew, K.L., McGee, R.C., Wells, M.S., and Kelleher-Andersson, J.A. (2011). Growth and differentiation of adult hippocampal arctic ground squirrel neural stem cells. J. Vis. Exp. (47), 2199.

Dunlop, R.A., Brunk, U.T., and Rodgers, K.J. (2009). Oxidized proteins: mechanisms of removal and consequences of accumulation. IUBMB Life *61*, 522–527.

Fabre, E., Conti, M., Paradis, V., Droupy, S., Bedossa, P., Legrand, A., Benoit, G., and Eschwege, P. (2002). Impact of different combined preservation modalities on warm ischemic kidneys: effect on oxidative stress, hydrostatic perfusion characteristics and tissue damage. Urol. Res. *30*, 89–96.

Fedorov, V.B., Goropashnaya, A.V., Stewart, N.C., Tøien, Ø., Chang, C., Wang, H., Yan, J., Showe, L.C., Showe, M.K., and Barnes, B.M. (2014). Comparative functional genomics of adaptation to muscular disuse in hibernating mammals. Mol. Ecol. *23*, 5524–5537.

Forreider, B., Pozivilko, D., Kawaji, Q., Geng, X., and Ding, Y. (2017). Hibernation-like neuroprotection in stroke by attenuating brain metabolic dysfunction. Prog. Neurobiol. *157*, 174–187.

Fukuda, T., Ewan, L., Bauer, M., Mattaliano, R.J., Zaal, K., Ralston, E., Plotz, P.H., and Raben, N. (2006). Dysfunction of endocytic and autophagic pathways in a lysosomal storage disease. Ann. Neurol. *59*, 700–708.

Geiser, F. (2004). Metabolic rate and body temperature reduction during hibernation and daily torpor. Annu. Rev. Physiol. *66*, 239–274.

Goldberg, A.L. (2003). Protein degradation and protection against misfolded or damaged proteins. Nature *426*, 895–899.

Gregersen, N., and Bross, P. (2010). Protein misfolding and cellular stress: an overview. Methods Mol. Biol. *648*, 3–23.

Grune, T., Reinheckel, T., and Davies, K.J. (1997). Degradation of oxidized proteins in mammalian cells. FASEB J. *11*, 526–534.

Guillaud, L., Bosc, C., Fourest-Lieuvin, A., Denarier, E., Pirollet, F., Lafanechère, L., and Job, D. (1998). STOP proteins are responsible for the high degree of microtubule stabilization observed in neuronal cells. J. Cell Biol. *142*, 167–179.

Hammond, J.W., Cai, D., and Verhey, K.J. (2008). Tubulin modifications and their cellular functions. Curr. Opin. Cell Biol. *20*, 71–76.

Hampton, M., Melvin, R.G., and Andrews, M.T. (2013). Transcriptomic analysis of brown adipose tissue across the physiological extremes of natural hibernation. PLoS ONE *8*, e85157.

Hindle, A.G., and Martin, S.L. (2013). Cytoskeletal regulation dominates temperature-sensitive proteomic changes of hibernation in forebrain of 13-lined ground squirrels. PLoS ONE *8*, e71627.

Iwata, A., Riley, B.E., Johnston, J.A., and Kopito, R.R. (2005). HDAC6 and microtubules are required for autophagic degradation of aggregated huntingtin. J. Biol. Chem. *280*, 40282–40292.

Jain, S., Keys, D., Martin, S., Edelstein, C.L., and Jani, A. (2016). Protection from apoptotic cell death during cold storage followed by rewarming in 13-lined ground squirrel tubular cells: the role of prosurvival factors X-linked inhibitor of apoptosis and PhosphoAkt. Transplantation *100*, 538–545.

Kapitein, L.C., and Hoogenraad, C.C. (2015). Building the neuronal microtubule cytoskeleton. Neuron *87*, 492–506.

Kiemer, L., Bendtsen, J.D., and Blom, N. (2005). NetAcet: prediction of N-terminal acetylation sites. Bioinformatics *21*, 1269–1270.

Laursen, W.J., Mastrotto, M., Pesta, D., Funk, O.H., Goodman, J.B., Merriman, D.K., Ingolia, N., Shulman, G.I., Bagriantsev, S.N., and Gracheva, E.O. (2015). Neuronal UCP1 expression suggests a mechanism for local thermogenesis during hibernation. Proc. Natl. Acad. Sci. USA *112*, 1607–1612.

Lee, J., Giordano, S., and Zhang, J. (2012). Autophagy, mitochondria and oxidative stress: cross-talk and redox signalling. Biochem. J. *441*, 523–540.

Liao, Y., Smyth, G.K., and Shi, W. (2013). The Subread aligner: fast, accurate and scalable read mapping by seed-and-vote. Nucleic Acids Res. *41*, e108.

Liu, D., Chan, S.L., de Souza-Pinto, N.C., Slevin, J.R., Wersto, R.P., Zhan, M., Mustafa, K., de Cabo, R., and Mattson, M.P. (2006). Mitochondrial UCP4 mediates an adaptive shift in energy metabolism and increases the resistance of neurons to metabolic and oxidative stress. Neuromolecular Med. *8*, 389–414.

Longair, M.H., Baker, D.A., and Armstrong, J.D. (2011). Simple Neurite Tracer: open source software for reconstruction, visualization and analysis of neuronal processes. Bioinformatics *27*, 2453–2454.

Love, M.I., Huber, W., and Anders, S. (2014). Moderated estimation of fold change and dispersion for RNA-seq data with DESeq2. Genome Biol. *15*, 550.

Maathuis, M.H., Leuvenink, H.G., and Ploeg, R.J. (2007). Perspectives in organ preservation. Transplantation *83*, 1289–1298.

Mangino, M.J., Tian, T., Ametani, M., Lindell, S., and Southard, J.H. (2008). Cytoskeletal involvement in hypothermic renal preservation injury. Transplantation *85*, 427–436.

Marion, D.W., Penrod, L.E., Kelsey, S.F., Obrist, W.D., Kochanek, P.M., Palmer, A.M., Wisniewski, S.R., and DeKosky, S.T. (1997). Treatment of traumatic brain injury with moderate hypothermia. N. Engl. J. Med. *336*, 540–546.

McAnulty, J.F. (2010). Hypothermic organ preservation by static storage methods: current status and a view to the future. Cryobiology *60* (3, Suppl), S13–S19.

McWilliam, H., Li, W., Uludag, M., Squizzato, S., Park, Y.M., Buso, N., Cowley, A.P., and Lopez, R. (2013). Analysis tool web services from the EMBL-EBI. Nucleic Acids Res. *41*, W597–600.

Meberg, P.J., and Miller, M.W. (2003). Culturing hippocampal and cortical neurons. Methods Cell Biol. *71*, 111–127.

Mertens, J., Paquola, A.C.M., Ku, M., Hatch, E., Böhnke, L., Ladjevardi, S., McGrath, S., Campbell, B., Lee, H., Herdy, J.R., et al. (2015). Directly reprogrammed human neurons retain aging-associated transcriptomic signatures and reveal age-related nucleocytoplasmic defects. Cell Stem Cell *17*, 705–718.

Mitchell, T., Rotaru, D., Saba, H., Smith, R.A., Murphy, M.P., and MacMillan-Crow, L.A. (2011). The mitochondria-targeted antioxidant mitoquinone protects against cold storage injury of renal tubular cells and rat kidneys. J. Pharmacol. Exp. Ther. *336*, 682–692.

Morin, P., Jr., and Storey, K.B. (2009). Mammalian hibernation: differential gene expression and novel application of epigenetic controls. Int. J. Dev. Biol. *53*, 433–442.

Nathaniel, T.I. (2008). Brain-regulated metabolic suppression during hibernation: a neuroprotective mechanism for perinatal hypoxia-ischemia. Int. J. Stroke *3*, 98–104.

Niemann, C.U., Feiner, J., Swain, S., Bunting, S., Friedman, M., Crutchfield, M., Broglio, K., Hirose, R., Roberts, J.P., and Malinoski, D. (2015). Therapeutic Hypothermia in Deceased Organ Donors and Kidney-Graft Function. N. Engl. J. Med. *373*, 405–414.

Penazzi, L., Bakota, L., and Brandt, R. (2016). Microtubule dynamics in neuronal development, plasticity, and neurodegeneration. Int. Rev. Cell Mol. Biol. *321*, 89–169.

Peretti, D., Bastide, A., Radford, H., Verity, N., Molloy, C., Martin, M.G., Moreno, J.A., Steinert, J.R., Smith, T., Dinsdale, D., et al. (2015). RBM3 mediates structural plasticity and protective effects of cooling in neurodegeneration. Nature *518*, 236–239.

Qiang, X., Yang, W.L., Wu, R., Zhou, M., Jacob, A., Dong, W., Kuncewitch, M., Ji, Y., Yang, H., Wang, H., et al. (2013). Cold-inducible RNA-binding protein (CIRP) triggers inflammatory responses in hemorrhagic shock and sepsis. Nat. Med. *19*, 1489–1495.

Quinones, Q.J., Ma, Q., Zhang, Z., Barnes, B.M., and Podgoreanu, M.V. (2014). Organ protective mechanisms common to extremes of physiology: a window through hibernation biology. Integr. Comp. Biol. *54*, 497–515.

Rauen, U., and de Groot, H. (1998). Cold-induced release of reactive oxygen species as a decisive mediator of hypothermia injury to cultured liver cells. Free Radic. Biol. Med. *24*, 1316–1323.

Reinhard, K., Mutter, M., Gustafsson, E., Gustafsson, L., Vaegler, M., Schultheiss, M., Müller, S., Yoeruek, E., Schrader, M., and Münch, T.A. (2016). Hypothermia promotes survival of ischemic retinal ganglion cells. Invest. Ophthalmol. Vis. Sci. *57*, 658–663.

Roberg, K., and Ollinger, K. (1998). Oxidative stress causes relocation of the lysosomal enzyme cathepsin D with ensuing apoptosis in neonatal rat cardiomyocytes. Am. J. Pathol. *152*, 1151–1156.

Schultheiss, M., Schnichels, S., Hermann, T., Hurst, J., Feldkaemper, M., Arango-Gonzalez, B., Ueffing, M., Bartz-Schmidt, K.U., Zeck, G., and Spitzer, M.S. (2016). Hypothermia protects and prolongs the tolerance time of retinal ganglion cells against ischemia. PLoS ONE *11*, e0148616.

Shen, D., Coleman, J., Chan, E., Nicholson, T.P., Dai, L., Sheppard, P.W., and Patton, W.F. (2011). Novel cell- and tissue-based assays for detecting misfolded and aggregated protein accumulation within aggresomes and inclusion bodies. Cell Biochem. Biophys. *60*, 173–185.

Skulachev, V.P. (1991). Fatty acid circuit as a physiological mechanism of uncoupling of oxidative phosphorylation. FEBS Lett. *294*, 158–162.

Song, Y., Kirkpatrick, L.L., Schilling, A.B., Helseth, D.L., Chabot, N., Keillor, J.W., Johnson, G.V., and Brady, S.T. (2013). Transglutaminase and polyamination of tubulin: posttranslational modification for stabilizing axonal microtubules. Neuron *78*, 109–123.

Speir, M.L., Zweig, A.S., Rosenbloom, K.R., Raney, B.J., Paten, B., Nejad, P., Lee, B.T., Learned, K., Karolchik, D., Hinrichs, A.S., et al. (2016). The UCSC Genome Browser database: 2016 update. Nucleic Acids Res. *44* (D1), D717–D725.

Staples, J.F. (2016). Metabolic flexibility: hibernation, torpor, and estivation. Compr. Physiol. *6*, 737–771.

Starkov, A.A., and Fiskum, G. (2003). Regulation of brain mitochondrial $H_2O_2$ production by membrane potential and NAD(P)H redox state. J. Neurochem. *86*, 1101–1107.

Storey, K.B., and Storey, J.M. (2010). Metabolic rate depression: the biochemistry of mammalian hibernation. Adv. Clin. Chem. *52*, 77–108.

Takahashi, K., and Yamanaka, S. (2006). Induction of pluripotent stem cells from mouse embryonic and adult fibroblast cultures by defined factors. Cell *126*, 663–676.

Taylor, M.J. (2006). Biology of Cell Survival in the Cold. In Advances in Biopreservation, J.G. Baust and J.M. Baust, eds. (CRC Press), pp. 15–62.

Tong, G., Endersfelder, S., Rosenthal, L.M., Wollersheim, S., Sauer, I.M., Bührer, C., Berger, F., and Schmitt, K.R. (2013). Effects of moderate and deep hypothermia on RNA-binding proteins RBM3 and CIRP expressions in murine hippocampal brain slices. Brain Res. *1504*, 74–84.

Trapnell, C., Pachter, L., and Salzberg, S.L. (2009). TopHat: discovering splice junctions with RNA-Seq. Bioinformatics *25*, 1105–1111.

Väremo, L., Nielsen, J., and Nookaew, I. (2013). Enriching the gene set analysis of genome-wide data by incorporating directionality of gene expression and combining statistical hypotheses and methods. Nucleic Acids Res. *41*, 4378–4391.

von der Ohe, C.G., Darian-Smith, C., Garner, C.C., and Heller, H.C. (2006). Ubiquitous and temperature-dependent neural plasticity in hibernators. J. Neurosci. *26*, 10590–10598.

Wallin, M., and Strömberg, E. (1995). Cold-stable and cold-adapted microtubules. Int. Rev. Cytol. *157*, 1–31.

Wang, L., Du, Y., Lu, M., and Li, T. (2012). ASEB: a web server for KAT-specific acetylation site prediction. Nucleic Acids Res. *40*, W376–W379.

Webb, B.C., and Wilson, L. (1980). Cold-stable microtubules from brain. Biochemistry *19*, 1993–2001.

Weber, K., Pollack, R., and Bibring, T. (1975). Antibody against tuberlin: the specific visualization of cytoplasmic microtubules in tissue culture cells. Proc. Natl. Acad. Sci. USA *72*, 459–463.

Wickham, H. (2009). ggplot2: Elegant Graphics for Data Analysis (Springer-Verlag New York).

Williams, D.R., Epperson, L.E., Li, W., Hughes, M.A., Taylor, R., Rogers, J., Martin, S.L., Cossins, A.R., and Gracey, A.Y. (2005). Seasonally hibernating phenotype assessed through transcript screening. Physiol. Genomics *24*, 13–22.

Wilson, C., and González-Billault, C. (2015). Regulation of cytoskeletal dynamics by redox signaling and oxidative stress: implications for neuronal development and trafficking. Front. Cell. Neurosci. *9*, 381.

Yamashita, H., Sato, Y., and Mori, N. (1999). Difference in induction of uncoupling protein genes in adipose tissues between young and old rats during cold exposure. FEBS Lett. *458*, 157–161.

Yates, A., Akanni, W., Amode, M.R., Barrell, D., Billis, K., Carvalho-Silva, D., Cummins, C., Clapham, P., Fitzgerald, S., Gil, L., et al. (2016). Ensembl 2016. Nucleic Acids Res. *44* (D1), D710–D716.

Yenari, M.A., and Han, H.S. (2012). Neuroprotective mechanisms of hypothermia in brain ischaemia. Nat. Rev. Neurosci. *13*, 267–278.

Zhang, T., and Ye, Y. (2014). The final moments of misfolded proteins en route to the proteasome. DNA Cell Biol. *33*, 477–483.

Zhang, Y., Pan, Y.-H., Yin, Q., Yang, T., Dong, D., Liao, C.-C., and Zhang, S. (2014). Critical roles of mitochondria in brain activities of torpid Myotis ricketti bats revealed by a proteomic approach. J. Proteomics *105*, 266–284.

Zhu, X., Bührer, C., and Wellmann, S. (2016). Cold-inducible proteins CIRP and RBM3, a unique couple with activities far beyond the cold. Cell. Mol. Life Sci. *73*, 3839–3859.

## STAR★METHODS

### KEY RESOURCES TABLE

| REAGENT or RESOURCE | SOURCE | IDENTIFIER |
|---|---|---|
| Antibodies | | |
| Mouse monoclonal anti-Poly-E-T (1:1000) | AdipoGen | Cat# AG-20B-0020-C100 |
| Mouse monoclonal anti-TUBB3 (1:1000) | R&D Systems | Cat# MAB1195 |
| Mouse monoclonal anti-OCT3/4 (1:500) | Santa Cruz | Cat# sc-5279 |
| Rabbit polyclonal anti-NANOG (1:500) | Cosmo Bio | Cat# RCAB0004P-F |
| Mouse monoclonal anti-ALBUMIN (1:500) | Cedarlane | Cat# CL2513A |
| Rabbit monoclonal anti-HNF4A (1:500) | Cell Signaling | Cat# 3113S |
| Rabbit polyclonal anti-DESMIN (1:500) | Thermo Fisher | Cat# RB9014P1 |
| Mouse anti-TNNT (1:500) | Thermo Fisher | Cat# MS295P0 |
| Rabbit polyclonal anti- Δ2-T (1:1000) | Millipore | Cat# AB3203 |
| Rabbit polyclonal anti-Poly-E-T (1:2000) | AdipoGen | Cat# AG-25B-0030-C050 |
| Rabbit polyclonal anti-TUBB3 (1:2000) | BioLegend | Cat# 802001 |
| Mouse monoclonal anti-TUBA (1:200) | Sigma | Cat# F2168 |
| Rabbit monoclonal anti-LAMP1 (1:1000) | Cell Signaling | Cat# 9091 |
| Rabbit polyclonal anti-VCP (p97) (1:1000) | Cell Signaling | Cat# 2648 |
| Mouse monoclonal anti-VCP (p97) (1:5000) | Fitzgerald | Cat# 10R-P104a |
| Mouse monoclonal anti-PSMB2 (1:1000) | Santa Cruz | Cat# sc-515066 |
| Mouse monoclonal anti-PSMB5 (1:1000) | Santa Cruz | Cat# sc-393931 |
| Mouse monoclonal anti-HSP60 (1:1000) | Santa Cruz | Cat# 4868 |
| Mouse monoclonal anti-HSP70 (1:1000) | Santa Cruz | Cat# sc-7298 |
| Mouse monoclonal anti-HSP90 (1:1000) | Santa Cruz | Cat# sc-13119 |
| Rabbit monoclonal anti-β-actin (1:1000) | Cell Signaling | Cat# 4970 |
| Rabbit polyclonal anti-cleaved Caspase-3 (1:500) | Cell Signaling | Cat# 9661 |
| Chicken polyclonal anti-GFP (1:1000) | Aves Labs | Cat# GFP-1020 |
| Rabbit polyclonal anti-RBM3 (1:1000) | Proteintech | Cat# 14363-1-AP |
| Rabbit polyclonal anti-CIRP (1:1000) | Proteintech | Cat# 10209-2-AP |
| Chemicals, Peptides, and Recombinant Proteins | | |
| Cell Culture Media Formulations & Reagents | This paper | N/A |
| B27 supplement minus insulin | Thermo Fisher | Cat# A1895601 |
| CHIR99021 | Tocris | Cat# 4423 |
| IWP4 | Tocris | Cat# 5214 |
| B27 supplement (complete) | Thermo Fisher | Cat# 17504044 |
| RPMI | Thermo Fisher | Cat# 11875093 |
| b-FGF | R&D Systems | Cat# 233-FB-025 |
| HGF | R&D Systems | Cat# 294-HG-005 |
| Hepatocyte Maintenance Media w/ Supplement | Lonza | Cat# MM250 |
| Oncostatin M | R&D Systems | Cat# 295-OM-010 |
| Propidium iodide | Tocris | Cat# 5135 |
| MG-132 (5 μM) | Enzo Life Sci. | Cat# ENZ-51035 |
| BAM15 (0.05-5 μM) | Tocris | Cat# 5737 |
| Protease inhibitor cocktail set III (PI) (1:500) | Millipore | Cat# 539134 |
| PYR-41 (5-10 μM) | Tocris | Cat# 2978 |
| Taxol (0.1 or 10 μM) | Tocris | Cat# 1097 |
| CellROX Green (1 μM) | Thermo Fisher | Cat# C10444 |

(*Continued on next page*)

*Continued*

| REAGENT or RESOURCE | SOURCE | IDENTIFIER |
|---|---|---|
| TMRE (50 nM) | Thermo Fisher | Cat# T669 |
| Ames' medium | Sigma | Cat# A1420 |
| TRIzol | Thermo Fisher | Cat#15596018 |
| LysoTracker Green DND-26 | Thermo Fisher | Cat# L7526 |
| RIPA lysis and extraction buffer | Thermo Fisher | Cat# 89900 |
| SYBR Green PCR Master mix | Thermo Fisher | Cat# 4309155 |
| BrightGreen Express 2X qPCR MasterMix-ROX | ABM | Cat# MasterMix-ER |
| Critical Commercial Assays | | |
| CytoTune iPS 2.0 Sendai Reprogramming Kit | Thermo Fisher | Cat# A16517 |
| Protein Oxidation Detection Kit | Millipore | Cat# S7150 |
| Proteostat Aggresome Detection Kit | Enzo Life Sci. | Cat# ENZ-51035 |
| LipoJet *in vitro* transfection kit | SignaGen Laboratories | Cat# SL100468 |
| RNeasy kit | QIAGEN | Cat# 74104 |
| TruSeq Stranded mRNA LT - Set A | Illumina | Cat# RS-122-2101 |
| NextSeq 500/550 High Output Kit v2 | Illumina | Cat# FC-404-2002 |
| Magic Red cathepsin B assay kit | Immuno-Chemistry Tech. | Cat# 938 |
| Click-iT lipid peroxidation imaging kit – Alexa Fluor 488 | Thermo Fisher | Cat# C10446 |
| Deposited Data | | |
| RNA-seq Data | This paper | GEO: GSE93935 |
| Experimental Models: Cell Lines | | |
| Ground Squirrel iPSC line (female) | This paper | GS-iPSC1 |
| Ground Squirrel iPSC line (female) | This paper | GS-iPSC3 |
| Ground Squirrel Cortical primary cultures (male/female) | This paper | N/A |
| Human iPSC line (female) | NIH NINDS Stem Cell Unit | SCU-i10 |
| Human iPSC line (male) | NIH NINDS Stem Cell Unit | SCU-i19 |
| Human iPSC line (male) | NIH NINDS Stem Cell Unit | SCU-i21 |
| Experimental Models: Organisms/Strains | | |
| Thirteen-lined ground squirrel | University of Wisconsin Oshkosh | N/A |
| Sprague Dawley Rats (males and females) | Charles River | RRID: RGD_737891 |
| Mouse: Wild-type C57BL/6 (males and females) | Jackson Labs | RRID: IMSR_JAX:000664 |
| Recombinant DNA | | |
| p*CMV6-XL5-TUBB3* | Origene | Cat# SC116313 |
| p*CMV6-Myc-DDK-Tubb3* | Origene | Cat# MR207181 |
| p*CMV6-UCP1-IRES2-eGFP* | GeneCopoeia | Cat# EX-C0618-M61 |
| p*CMV6-UCP2-IRES2-eGFP* | GeneCopoeia | Cat# EX-M0658-M61 |
| Software and Algorithms | | |
| MATLAB rev.2015a | Mathworks | https://www.mathworks.com/ |
| JMP | SAS | https://www.jmp.com/en_us/home.html |
| MC Rack | MultiChannel Systems | https://www.multichannelsystems.com/software/mc-rack |
| Plexon Offline Sorter v.3.3.5 | Plexon Inc. | https://plexon.com/products/offline-sorter/ |
| ImageJ Gel Analysis tool | NIH | https://imagej.nih.gov/ij/ |
| ImageJ (Simple Neurite Tracer plugin) | (Longair et al., 2011) | https://imagej.net/Simple_Neurite_Tracer |
| Bcl2fastq Conversion Software v2.19.1 | Illumina | https://support.illumina.com/downloads/bcl2fastq-conversion-software-v2-19.html |
| TopHat v2.1.1 | (Trapnell et al., 2009) | https://ccb.jhu.edu/software/tophat/index.shtml |

(*Continued on next page*)

*Continued*

| REAGENT or RESOURCE | SOURCE | IDENTIFIER |
|---|---|---|
| Rsubread Package | (Liao et al., 2013) | http://bioconductor.org/packages/release/bioc/html/Rsubread.html |
| DESeq2 | (Love et al., 2014) | https://bioconductor.org/packages/release/bioc/html/DESeq2.html |
| Ensembl database (spetri2) | (Yates et al., 2016) | https://useast.ensembl.org/index.html |
| CLUSTAL Omega | (McWilliam et al., 2013) | https://www.ebi.ac.uk/Tools/msa/clustalo/ |
| NetAcet 1.0 Server | (Kiemer et al., 2005) | http://www.cbs.dtu.dk/services/NetAcet/ |
| ASEB | (Wang et al., 2012) | https://bioconductor.statistik.tu-dortmund.de/packages/2.12/bioc/html/ASEB.html |
| piano | (Väremo et al., 2013) | https://bioconductor.org/packages/release/bioc/html/piano.html |
| ggplot2 | (Wickham, 2009) | https://cran.r-project.org/web/packages/ggplot2/index.html |

## CONTACT FOR REAGENT AND RESOURCE SHARING

Further information and requests of reagents can be directed to and fulfilled by the Lead Contact, Dr. Wei Li (liwei2@nei.nih.gov). The following materials: GS-iPSC1 and GS-iPSC3 (13-lined Ground Squirrel iPSC lines) are properties of U.S. federal government and may be shared with research organizations under an MTA.

## EXPERIMENTAL MODEL AND SUBJECT DETAILS

### Animals

Thirteen-lined ground squirrels used in this study were maintained in the University of Wisconsin Oshkosh animal facility and housed in seasonally-varying light/dark cycles matching ambient for that location. All animal procedures were approved by the Institutional Animal Care and Use Committee of the University of Wisconsin Oshkosh and conform to the provisions of the Animal Welfare Act (NIH/DHHS) and the Association for Assessment and Accreditation of Laboratory Animal Care (AAALAC). Cortical tissues from 4 GS pups (1 female and 1 male at postnatal day 0; 1 female and 1 male at postnatal day 2) were provided courtesy of Prof. Dana Merriman at the University of Wisconsin Oshkosh. Male and female C57BL/6 mice and Sprague-Dawley rats were maintained in the National Institute of Neurological Disorders and Stroke (NINDS) animal facility and housed in a 12-hr light/dark cycle. All animal procedures were approved by the Institutional Animal Care and Use Committee of the National Eye Institute (NEI)/NINDS and conform to the provisions of the Animal Welfare Act (NIH/DHHS). Post-mortem rat retinas were obtained from healthy adult rats of 2-6 months old and provided by the animal facility of NINDS. Post-mortem mouse kidneys were obtained from healthy adult mice of 2-12 months old and provided by the animal facility of NINDS.

### Primary Cultures

Cortical tissues from postnatal day 0-2 (P0-2) GS pups (female) were dissected and dissociated using a neural tissue dissociation kit (Miltenyi Biotech, San Diego, CA). Neural precursor cells (NPCs) were then purified with magnet-activated cell sorting using magnetic anti-PSA-NCAM microbeads, myelin removal beads, and FcR blocking reagent (Miltenyi Biotech, San Diego, CA). Primary cultures of rat (embryonic day 18) and GS (P0-2) cortical neurons were differentiated from rat and GS NPCs following the protocol described in (Meberg and Miller, 2003), and subjected to the same temperature experiments as GS and human iPSC-neurons (described in a later section). Cells were maintained at 37°C with 5% $CO_2$ unless otherwise specified.

## METHOD DETAILS

### Reprogramming of neonatal GS NPCs into iPSC colonies

All cell culture media reagents were used as directed in the manufacturer's instructions unless otherwise specified; the reagents are listed in Table S1. The purified P0-2 primary GS NPCs were expanded in 5% Matrigel-coated dishes at 37°C in NPC medium until 70%–80% confluence was reached. The NPCs were then transfected with the Cytotune-iPS 2.0 Sendai Reprogramming kit (Thermo Fisher Scientific, Waltham, MA) for 24 hours. The transfected NPCs were dissociated by accutase digestion and passaged into new 5% matrigel-coated wells at a 1:3 ratio in iPSC maintenance medium. After 5-7 days, flat colonies emerged and were manually picked or lifted off with dispase digestion, mechanically dissociated with gentle pipetting, and passaged to a new Matrigel-coated culture well. Note: Due to the limited availability of newborn GS pups from which the GS NPCs were derived, the two GS iPSC lines

(GS-iPSC1 and GS-iPSC3) that were successfully established were both female. Thus, an analysis of the influence or association of sex on the results of the study was not performed. Nonetheless, primary GS cortical cultures from both male and female pups did not reveal notable sex-dependent differences in our experiments.

### Validation of GS iPSCs

GS iPSC samples were sent for G-banding karyotyping to assess genomic stability - chromosome counts and images provided by Cell Line Genetics (Madison, WI) (See Figure S1D). Pluripotency of GS iPSC colonies was characterized by alkaline phosphatase staining and OCT3/4/NANOG immunostaining (antibodies listed in the Key Resources Table). Using primers specific for the expression of 3 pluripotent marker genes (Pou5f1, Nanog, Sox2) and 10 differentiation markers (Dppa5, Pdx1, Nestin, Sox17, Otx2, Tp63, Foxa2, Gata4, Afp, Brachyury) we confirmed by qRT-PCR the pluripotency of the GS iPSC colonies (data not shown).

The *in vitro* pluripotent status of GS iPSCs was also evaluated by their ability to differentiate into cell types from all 3 germ layers:

For Mesoderm differentiation: colonies were plated in a 6-well plate and the media was changed to RPMI containing 2% B27 without insulin and 12 μM CHIR99021. After another 24 hr the media was replaced with RPMI containing 2% B27 supplement minus insulin and 5 μM IWP4. 48 hr later the media was replaced with RPMI containing 2% B27 supplement (complete). Hereafter the media was changed every 3-4 days. Beating cardiomyocytes appeared around 6-10 days following initiation of the mesoderm differentiation protocol.

For Endoderm differentiation: colonies were plated in a 6-well plate and the medium was changed to RPMI and supplemented with 2% B27 and 100ng/ml Activin A. The medium was changed after 2-3 days. On day 5, the medium was changed to RPMI containing 2% B27 supplement and 10ng/ml b-FGF. The medium was changed after 2-3 days. On day 10, the medium was changed to RPMI containing 2% B27 supplement, and 20ng/mL HGF. On day 15, the medium was changed to Lonza Hepatocyte Culture Medium containing 20ng/ml oncostatin M. The medium was changed after 2-3 days. Cells were fixed and stained for HNF4A and Albumin.

For ectoderm differentiation: See Neuronal differentiation of human and GS iPSCs, and rat cortical primary cultures.

Pluripotency was also verified *in vivo* using a standard teratoma formation assay (Applied StemCell, CA, USA).

### Neuronal differentiation of human and GS iPSCs, and rat cortical primary cultures

Three different human iPSC-derived NPC lines (2 male – SCU-i19, SCUi21, and 1 female – SCU-i10) were obtained from the Stem Cell Unit of the NINDS, courtesy of Dr. Barbara Mallon. Human and GS NPCs were first expanded in NPC medium for 3 days and then switched to neural differentiation medium (NDM) (Table S1) for at least 7 days resulting in a population of neurons and support cells. Experimental results were verified in all three human NPC lines. For GS neuronal differentiation, the first 2 days required GS NDM, afterward the medium was changed to human NDM.

### Evaluation of microtubule cold-stability

The temperature-dependent experiments in this study were performed at ambient $CO_2$ concentration, which required the use of hibernate-medium (Table S1) to maintain the physiological pH. Experiments were conducted by first incubating cultured neurons (human iPSC-derived, GS iPSC-derived, GS primary, or rat primary cultures) or dissected retinas of adult rats in hibernate-medium for 60 min at room temperature. During this preparation time, drug treatments (see Chemicals, Peptides, and Recombinant Proteins, Key Resources Table) were introduced to test their effects on microtubule cold-stability. The cell culture dishes were then kept in an ambient 37°C incubator, or in a 4°C refrigerator. The cooling strategy in our experiments is comparable to conventional static tissue/organ cold storage (McAnulty, 2010; Mitchell et al., 2011) and another cell culture-based study (Rauen and de Groot, 1998). Cooling of the core body temperature of hibernating GSs transitioning from interbout arousal to torpor is provided in Figure S1E. The pH of hibernate-medium was stable and maintained the pH between 7.0 and 7.4 even after 16-hr incubation at 4°C.

### Multielectrode array (MEA) measurements

All experiments were carried out under dim red light. Rat retina explants were removed and cut into smaller pieces in hibernate-medium, and divided into different treatment groups for pre-incubation with drugs promoting microtubule cold-stability or a DMSO vehicle control at room temperature for 30 min. The cold-exposed groups were incubated in the refrigerator, while the fresh control samples were incubated on the bench in dark at room temperature. It has been shown that keeping enucleated eyes under hypothermic and ischemic conditions extends retinal viability *in vitro* (Reinhard et al., 2016; Schultheiss et al., 2016), as limited access to oxygen and nutrients might reduce mitochondrial metabolism and hence ROS production. Here we allowed the rat retinas to have full access to nutrients and oxygen in all experimental groups, hence low temperature was the only cause of stress in our experiments. After 4- or 24-h incubation, the cold-exposed retinal explants were placed on the bench for 10-15 min, and washed twice with fresh hibernate-medium. Retinal explants from all groups were then transferred to oxygenated (95% $O_2$/5% $CO_2$) bicarbonate-buffered AMES medium at room temperature. The sclera and RPE were removed prior to flat mounting the neural retina with the ganglion cell (RGC)-side facing down onto the MEA.

During MEA recording, the neural retinas were perfused with 95% $O_2$/5% $CO_2$-balanced AMES at 37°C to measure the spontaneous firing activity of the rat RGCs over the course of 15 min. To assess light responsiveness of the rat retina explants, the tissue was exposed to approximately 1 s flashes of light from either a bright white LED (Mightex, Pleasanton, CA) or a halogen lamp (OSRAM, Germany). For each retina, light-driven ganglion cell activity (action potential firing) was elicited in response to six flashes

of light that were spaced at approximately either 10 or 15 s intervals. After the recording, the rat retinal explants were fixed with 4% paraformaldehyde for 2 h and then immunostained for neuronal tubulins. For MEA data processing and analyses, the firing spikes of RGCs were first filtered and recorded in MC Rack with a high-pass filter set at 200 Hz, a low-pass filter set at 3000 Hz, and the automatic standard deviation for spike detection threshold was set at −6. To remove false positives and to group spikes into clusters corresponding to individual cells, spike waveforms were sorted using Plexon Offline Sorter v.3.3.5 (Plexon Inc., Dallas, TX). Spikes were automatically clustered into a maximum of eight units (cells) per electrode using the built-in K-means clustering algorithm. The analysis and identification of light responsiveness was performed in MATLAB rev.2015a (The Mathworks, Natick, MA). Briefly, spike times were binned at 200 ms intervals, and the firing rates observed for a given cell during the first bin of each light flash were statistically compared to those during non-stimulated intervals. A cell was considered light-responsive if 1) the stimulated spike rate was larger than the mean baseline firing rate and 2) the outcome of a two-tailed, unequal variance t test of these spike rates yielded a $p$-value < 0.01. This test underestimates the number of light-responsive cells because it detects ON, but not OFF light responses. OFF responses were clearly visible in most MEA recordings, but they constituted a minority of cell types and were not quantified here.

### Western blotting and immunostaining

All antibodies are listed in the Key Resources Table. RIPA buffer was used to lyse the cells and extract proteins (Thermo Fisher, Waltham, MA). Total proteins or proteins in the soluble fraction after standard centrifugation removing precipitates and debris were run on SDS-PAGE. Standard protocols were used for western blotting and immunostaining. For immunostaining of oxidized proteins, fixed cells were first incubated with 2,4-dinitrophenylhydrazine (DNPH), then stained with an antibody recognizing the DNPH-protein complex (Protein oxidation detection kit, see Key Resources Table). All immunostaining and live cell confocal images were captured on a Zeiss LSM 510 system (Zeiss, Oberkochen, Germany). Western blots were quantified with the ImageJ Gel Analysis tool.

### RNA-sequencing

GS and two different lines of human iPSC-neuronal cultures were maintained and prepared as described above. Experiments were conducted by first replacing NDM with fresh hibernate-medium and allowing the cultures to sit at room temperature for 30 min. GS neuronal cultures from 2 iPSC lines, and human neuronal cultures from 2 iPSC-NPC lines (SCU-i19 and SCU-i21) were used. The neuronal cultures from each cell line were divided into two groups: one was incubated in the refrigerator (4°C) and the other in an ambient 37°C incubator. Two incubation time points, 1 hr and 4 hr, were selected. At the end of cold-exposure, cells were collected and lysed in TRIzol (Thermo Fisher, Waltham, MA), total RNA was isolated and purified with miRNeasy kit (QIAGEN, Hilden, Germany). TruSeq Stranded mRNA Library Prep Kit was used to generate the sequencing libraries (Illumina, San Diego, CA) following the manufacturer's instructions. Briefly, 500 ng of total RNA was used for mRNA selection. After the reverse transcription to 1$^{st}$ strand cDNA, strand info was reserved during 2$^{nd}$ strand synthesis. The dsDNA fragments then had the addition of a single 'A' base and subsequent ligation of the adaptor. The products were then purified and enriched with PCR to create the final cDNA library. The cluster generation and single indexed pair-end (2X75) sequencing was run on NextSeq 500 with the NextSeq 500 High Output Kit v2 (150 cycles). Up to 12 barcoded samples were pooled for one single run with Q30 > 85% and at least 30M passed filter reads per sample. The raw base call (.bcl) files were converted to demultiplexed fastq files with Bcl2fastq v2.19.1 for data analysis.

### Mapping, quantification and differential expression analysis of RNA-seq data

After adaptor trimming, raw reads were assessed using the FastQC toolset (http://www.bioinformatics.babraham.ac.uk/projects/fastqc). Reads from different cell lines were aligned to the GS genome (Ensembl spetri2) (Yates et al., 2016) or to the human genome (UCSC hg19) (Speir et al., 2016) (http://genome.ucsc.edu/) separately with TopHat v2.1.1 (Trapnell et al., 2009) and allowed up to two mismatches per read for final read alignments. The complete parameter list for Tophat is "tophat2 -r 150 -g 20–no-coverage-search–library-type fr-firststrand." The statistics on the raw reads and alignments are shown in sheet 'Mapping Statistics', Data S3. For quantification of gene expression, only the reads aligned to exons uniquely were counted using the R Subread package (Liao et al., 2013). A gene was included in further analysis if the maximum count-per-million > 3 within any included samples. Given the pairwise design of the experiments, negative binomial GLM fitting and testing for the effect of treatment by control of the effect of different cell lines were performed with embedded functions in DESeq2 (Love et al., 2014). P values from differential expression tests were adjusted using the Benjamini-Hochberg procedure for multiple hypothesis testing.

### Functional enrichment analysis of altered transcripts

Gene Ontology (GO) analysis was performed based on hypergeometric test using Piano package (Väremo et al., 2013), with the gene list of interest as foreground, and all identified genes as background. The annotation of gene to GO terms was retrieved and localized from Ensembl database.

### Tubulin protein sequence homology analysis

Tubulin protein sequences for genes (*TUBA1C, TUBB2A, TUBB2B, TUBB/TUBB5, TUBA4A, TUBB3, TUBB4A, and TUBB6*) of human, mouse, rat and 13-lined ground squirrel were obtained from Uniprot database (2015) and aligned using CLUSTAL Omega program (McWilliam et al., 2013). Canonical protein sequences were used when multiple isoforms were available.

### Acetylation prediction analysis of tubulin proteins

For all tubulin proteins mentioned above, we performed N-terminal and lysine acetylation events prediction using NetAcet (Kiemer et al., 2005) and ASEB (Wang et al., 2012) separately. During prediction, complete protein sequences were submitted directly. In ASEB analysis, all available lysine acetylation transferases (KAT) families were explored. K-sites with $p < 0.05$ were identified as acetylated.

### Live cell imaging of mitochondrial membrane potential (TMRE)

GS and human iPSC-neuronal cultures were prepared as described above. Experiments were conducted by first removing the NDM and replacing it with hibernate-medium containing 50 nM TMRE (Thermo Fisher, Waltham, MA; see Key Resources Table). At this time, 1) 0.1 μM BAM15 or 2) 1:500 dilution of protease inhibitor cocktail III (Millipore-Sigma, Darmstadt, Germany) were delivered to the two drug treatment groups. Cells were returned to an ambient 37°C incubator for an additional 25 min. Additional hibernate-medium matching these treatment conditions was stored in 50 mL conical tubes in either a 45°C water bath or on ice to serve as a perfusion medium reservoir. Prior to imaging, TMRE-containing medium was discarded and replaced with fresh pre-warmed hibernate-medium. During the Z stack time-lapse confocal imaging, the culture dish was continuously perfused; first with medium from the 45°C reservoir for 5 min, and then switched to the ice-cold reservoir. This manipulation reduced the temperature of the medium in the culture dish to 10°C (the lowest temperature the perfusion system could attain). Cells in the field of view were refocused, and the same Z stack, time-lapse confocal images were taken for another 5 min. A maximum intensity projection of the Z stack images was produced for data analysis. At least 5 different well-focused imaged cells per experiment were measured. We corrected for temperature-dependent TMRE fluorescence increases under the assumption that the total TMRE molecules absorbed into each cell should remain relatively constant within the 10-min imaging duration. Thus, we initially selected the whole cell area as the region of interest (ROI) to estimate the temperature dependent contribution of the TMRE dye's fluorescence. To do this, we calculated the average TMRE fluorescence intensity from 10 frames of the 10°C recording and divided that by the average TMRE fluorescence intensity from 10 frames of the 37°C recording ($F_{c\text{-}10}/F_{c\text{-}37}$). The mitochondrial areas from the same cells were then selected as ROIs to measure the mitochondrial TMRE intensity at 37°C ($F_{m\text{-}37}$) and 10°C ($F_{m\text{-}10}$). The corrected mitochondrial TMRE intensity at 10°C was calculated using the following equation: $F_{c.m\text{-}10} = F_{m\text{-}10}/(F_{c\text{-}10}/F_{c\text{-}37})$. The percentage change in mitochondrial TMRE intensity change at 10°C was thus calculated as: $(F_{c.m\text{-}10} - F_{m\text{-}37})/ F_{m\text{-}37} \times 100\%$.

### Live cell imaging of ROS production (CellROX-green)

GS and human iPSC-neuronal cultures were prepared in two groups and pretreated with 1 μM CellROX-green (Thermo Fisher, Waltham, MA; see Key Resources Table) with the appropriate drug treatments or vehicle as described above. To explore the influence of cold stress on ROS production, cells were either maintained at 37°C (group 1; as normal controls) or exposed to 4°C (group 2). Cells in group 2 were maintained for 30-min at 37°C, acclimated to room temperature on the bench for 5 min before being placed in a 4°C refrigerator for 30 min; they were then gradually rewarmed at room temperature on the bench for 5 min prior to returning to 37°C. Z stack confocal images were then obtained from the two groups at 37°C. Specifically, since CellROX-green only becomes fluorescent upon oxidation and DNA-binding, this method avoids temperature-dependent dye fluorescent artifacts that accompany imaging at different temperatures while recording the cumulative production of ROS. Maximum intensity projections of the Z stack images were produced for data analysis. At least 5 different well-focused imaged areas from each experiment were measured. The percentage change in ROS production at 4°C was thus calculated as: $(F_2 - F_1)/ F_0 \times 100\%$, in which $F_2$ and $F_1$ are the mean CellROX-green fluorescent intensity of the different areas from cultures in group 2 ($F_2$) or group 1($F_1$) at the end of the temperature experiment, while $F_0$ is the mean CellROX-green fluorescent intensity of the different areas from cultures in both group 1 and 2 at the end of the initial 30-min incubation at 37°C. Preliminary experiments indicated that prior to low temperature incubation (time 0), group 2 had similar CellROX-green fluorescent intensity to that of group 1 (data not shown).

### Live cell imaging of lysosomes using Magic Red and DND-26

GS and Human iPSC-neuronal cultures were prepared in two groups and incubated with hibernate-medium containing Magic Red (1:1000; ImmunoChemistry Technologies, Bloomington, MN) at 37°C for 25 min, followed by the addition of LysoTracker Green DND-26 (50 nM; Thermo Fisher, Waltham, MA; see Key Resources Table) for 5 min. The dye-containing medium was then replaced with fresh hibernate-medium, and one group of cultures was incubated at 4°C for 1, 4 or 16 hr, while the other group remained at 37°C serving as normal controls. The cold-exposed group was subjected to confocal imaging at various temperatures (10°C, room temperature, or 37°C), while the control group was imaged at either room temperature or 37°C. These imaging conditions did not influence significantly the occurrence of the lysosomal membrane permeability (LMP). Magic Red becomes fluorescent after being cleaved by the lysosomal protease cathepsin B, while DND-26 is an acidotropic probe that accumulates in the acidic lysosomal vesicles. When LMP occurs, Magic Red and DND-26 signals diffuse to the cytoplasm of the affected cells. In this work, we determined that cells have LMP if they contain a single Magic Red-stained particle of diameter > 5 μm, which is about the size of the neuronal cell nucleus.

### Neurite tracing

Cultured neurons or rat retinal explants with or without treatments were fixed with 4% paraformaldehyde, permeabilized and washed with 0.1% Triton X-100 in phosphate buffered saline and stained by antibodies against TUBB3. TUBB3+ neurite or RGC dendrite

paths in images of 188.94 × 188.94 $\mu m^2$ from human iPSC-neuronal cultures and images of 67.48 × 67.48 $\mu m^2$ from rat whole-mount retinas were traced with the 'Simple Neurite Tracer' plugin (Longair et al., 2011), ImageJ.

### Detection of protein aggregates

After treatments, cultured neurons were fixed with 4% paraformaldehyde for 10 min and then permeabilized and washed with 0.1% Triton X-100 in phosphate buffered saline. Protein aggregates were visualized by a dye that intercalates into the denatured and aggregated proteins and becomes fluorescent (Proteostat aggresome detection kit, Enzo, Farmingdale, NY; see Key Resources Table) (Shen et al., 2011). For accumulation of protein aggregates on the neuronal microtubules, cells were stained with TUBB3 antibody and the protein aggregate dye, and images (188.94 μm x 188.94 μm) were taken. In each image, the number of protein aggregates residing on the microtubules was counted and divided by the total length of the TUBB3+ neurite paths.

### Evaluation on mouse kidneys after cold storage

Healthy adult C57BL/6J mice under deep anesthetization were first gently perfused by warm 0.9% NaCl solution and hence sacrificed, then the mice were perfused a second time with standard University of Wisconsin Solution for human organ cold storage (UW solution; see Table S1) in control group, or UW solution supplemented with 0.2 μM BAM15/1:200 dilution of protease inhibitor cocktail III in treatment group. In experiments evaluating lipid peroxidation during cold storage, linoleamide alkyne (from the Click-iT lipid peroxidation imaging kit; Thermo Fisher, see Key Resources Table) was also included during perfusion. Mouse kidneys from the two groups were then removed and transferred to 12-well plates containing UW solution + linoleamide alkyne, or UW solution + BAM15/PI + linoleamide alkyne, and set at room temperature for 30 min. Fresh controls were fixed with 4% paraformaldehyde after this stage, while kidneys in cold-control group and treatment group were then incubated at 4°C. To evaluate tubulin re-polymerization following 24-hr cold storage, the kidneys were placed at room temperature for 10 min, rinsed twice with fresh warm UW solution only, and then rewarmed in an ambient 37°C incubator for 30 min. The kidneys were then fixed with 4% paraformaldehyde for 2 hr, processed for cryosections and immunostained for α-tubulin TUBA (see Key Resources Table). To evaluate lipid peroxidation following 24-hr cold storage, kidneys were fixed and processed according to the manufacturer's instruction (see Key Resources Table). To evaluate cell apoptosis following 72-hr cold storage, the kidneys were fixed and immunostained for cleaved Caspase-3 (see Key Resources Table).

## QUANTIFICATION AND STATISTICAL ANALYSIS

MATLAB (Mathworks) and JMP Statistical Software (SAS) were used for data and statistical analysis. In this work, all experiments were repeated as indicated by 'n' provided in the Figure legends. The 'n' number represents experimental replications for each line of cultured cells, number of animals studied, or number of cells studied in karyotyping (Figure S1D). The total numbers of cell lines used in each experiment were also provided in the legends. Error bars in all figures indicate standard error of the mean. Neurons derived from 2 GS iPSC lines and 3 human iPSC-NPC lines (SCU-i10, SCU-i19 & SCU-i21; Barbara Mallon, Stem Cell Unit, NINDS) were used. First, to determine if temperature had a significant effect, data from the normal control group and cold-exposed control group were analyzed by Student's t test. Second, to determine the significance of the effects of various treatments for the same duration, data from the treatment groups and cold-exposed control group were analyzed by ANOVA plus Tukey post hoc test. Statistical significance is defined as: * $p < 0.05$, ** $p < 0.01$ and *** $p < 0.001$. No inclusion criterion was used. The following exclusion criteria were used: For any given experiment, if the normal control (at 37°C) showed abnormal tubulin morphology, large numbers of dead cells, limited spontaneous RGC activity as evaluated by MEA or poor kidney histology, then the entire set of cultured cells or animal tissues/organs were removed from further analysis.

## DATA AND SOFTWARE AVAILABILITY

RNA-seq data were at https://www.ncbi.nlm.nih.gov/geo/query/acc.cgi?acc=GSE93935 with access code GEO: GSE93935. No software was generated for this project.

Cell

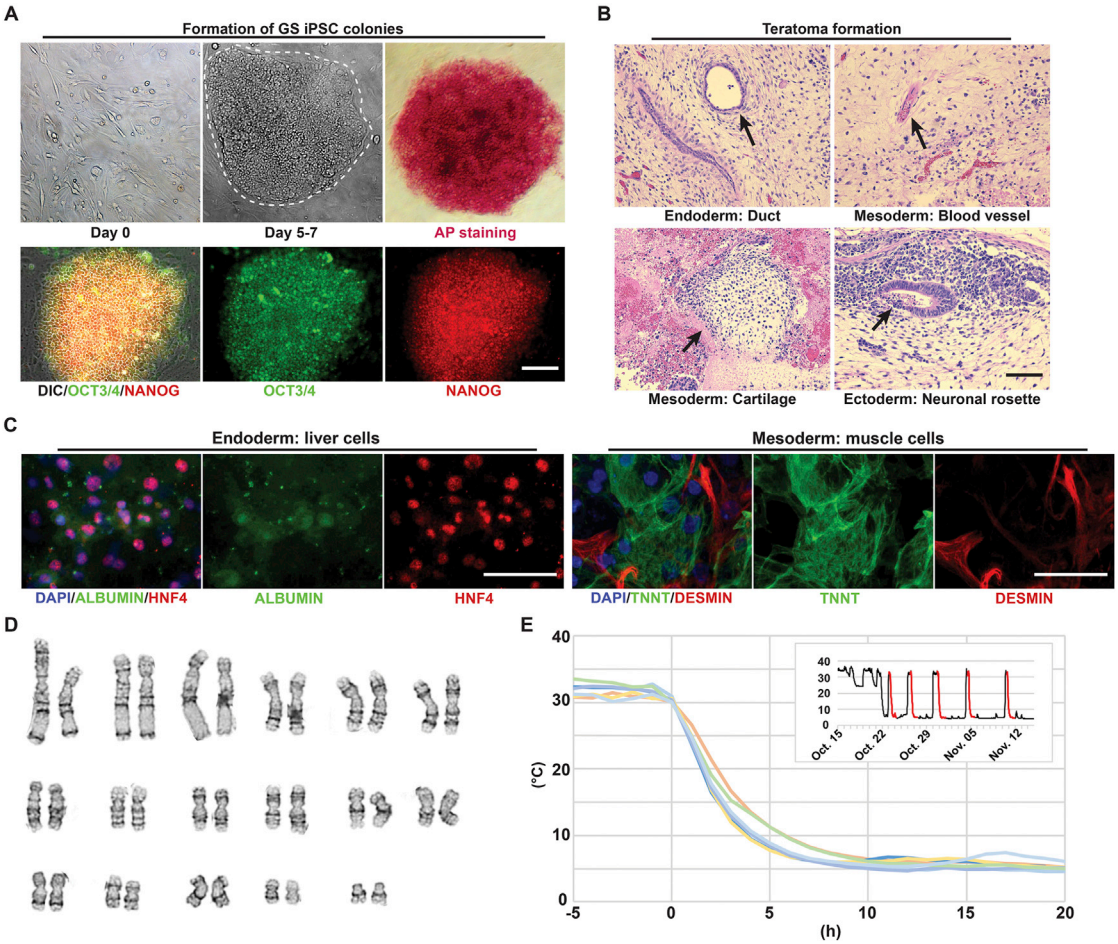


**Figure S1. Characterization of Ground Squirrel Induced Pluripotent Stem Cells, Related to Figure 1**

(A) Formation and characterization of ground-squirrel induced pluripotent stem cell (GS iPSC) colonies (see STAR Methods). Colonies were positive for pluripotency assays such as alkaline phosphatase (AP) staining and immunostaining of the pluripotency markers OCT3/4 (green) and NANOG (red). Scale bar: 150 μm.

(B) Hematoxylin and eosin stained cross-sections of collected teratomas (see STAR Methods) demonstrating differentiation of GS iPSCs into exogenous tissues (arrows) representing all three germ layers. Scale bar: 150 μm.

(C) Left: GS iPSCs were differentiated into liver cells, a signature cell type of the endoderm, and stained by antibodies against liver cell markers ALBUMIN (green), HFN4 (red) and the cell nuclear dye DAPI (blue). Right: GS iPSCs were differentiated into muscle cells, a signature cell type of the mesoderm, and stained by antibodies against muscle cell markers Troponin T (TNNT, green), DESMIN (red) and DAPI (blue). Scale bars: 50 μm.

(D) Representative G-banded karyotype of GS iPSCs (n = 13 cells).

(E) Overlaid averaged temperatures during re-entrances into torpor from 7 GSs in one winter season (temperatures logged hourly using implanted iButton transponders). Each line represents a different animal. Records are aligned to the entrance into torpor, where 0 h is the timestamp before the first temperature drop > 3°C. The inset demonstrates the first month of hibernation from an example GS, highlighting torpor re-entrances used for this analysis in red. In 5 of 7 GSs, the body temperatures reached 10°C within 4-5 hr, and all 7 GSs reached their stable hibernation temperature in about 10 h, which is still within the time range of our cultured cell and organ cold storage experiments.

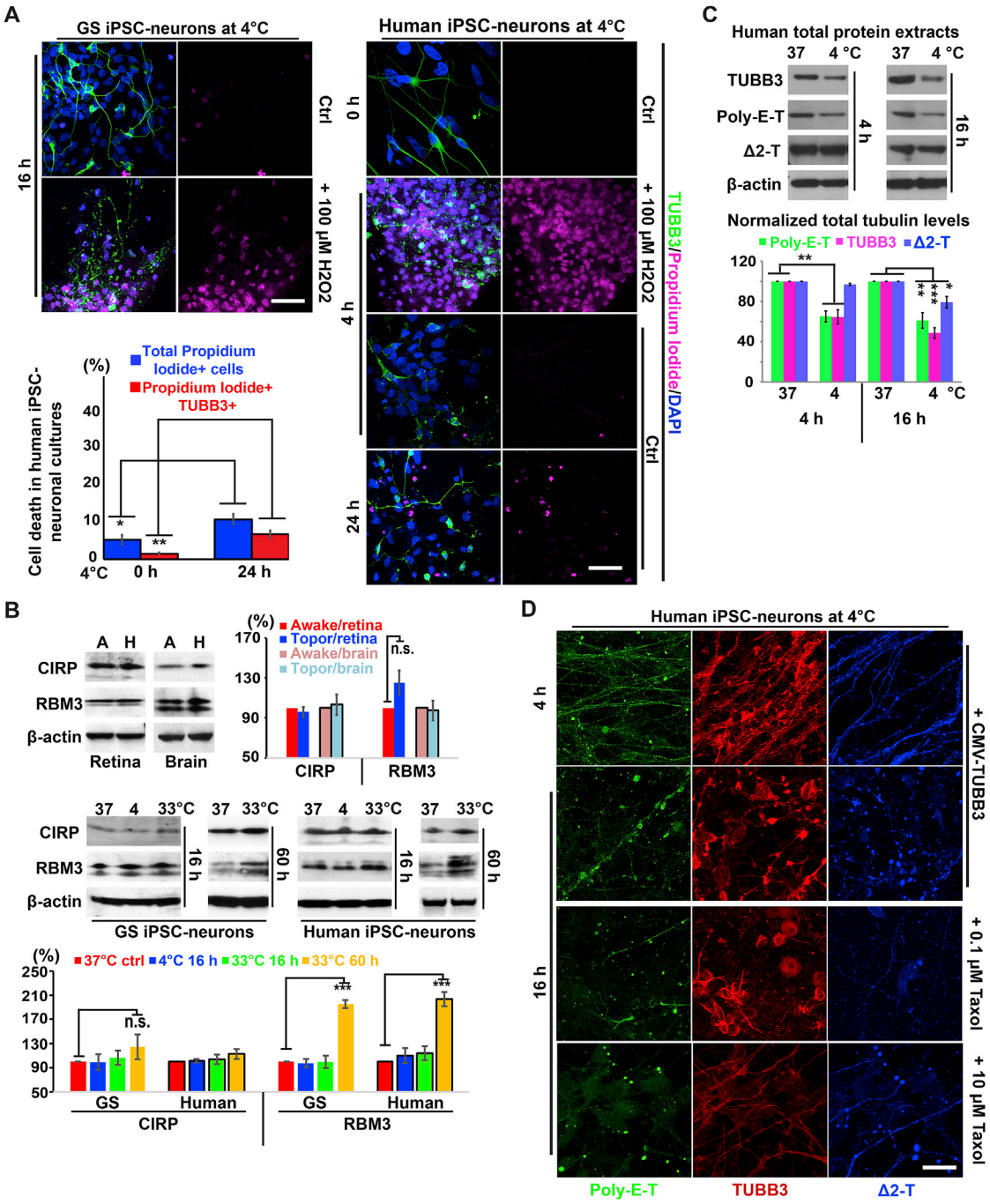


**Figure S2. Effects of TUBB3 Overexpression and Taxol on Protecting Neuronal Microtubules of Human iPSC-Neurons against Cold Stress, Related to Figure 2**

(A) Cold-induced microtubule disruption is not a secondary effect of cell death (n = 5 experiments each from 2 GS and 3 human cell lines). Upper Left: GS iPSC-neurons maintained their long neurites (TUBB3, green) and viability (dying cells become permeable and stained by Propidium Iodide, magenta) during 16-hr incubation at 4°C, but failed to survive when $H_2O_2$ (100 μM) was added. Right: In contrast, 4-hr incubation at 4°C disrupted most neurites in human iPSC-neurons without increasing cell death, while extended 24-hr incubation caused a small increase in dead cells from 5% to 11% (lower left; Student's t test for two-group comparisons; *p < 0.05; **p < 0.01). Scale bars: 40 μm. Error bars indicate SEM.

(B) Western blots and quantification of RBM3 and CIRP proteins in awake and hibernating (torpor) GS retinas (n = 12 animals each), GS brains (n = 5 animals each), GS iPSC-neurons (n = 5 experiments from 2 cell lines for each group) and human iPSC-neurons (n = 5 experiments from 2 cell lines for each group). Note that RBM3 proteins were upregulated in cultured neurons at mild hypothermia (33°C) with extended (60 hr) incubation time, but not in other conditions tested

*(legend continued on next page)*

(Student's t test for two-group comparisons; n.s., not significant, $p > 0.05$; ***$p < 0.001$). A, proteins extracted from active GS with a body temperature of 36°C; H, proteins extracted from hibernating GS with a body temperature of 2-4°C. Error bars indicate SEM.

(C) Western blots and quantification of total TUBB3, poly-E-T and Δ2-T proteins in human iPSC-neurons following 4- or 16-hr cold exposure (n = 5 experiments from 2 cell lines; Student's t test for two-group comparisons; *$p < 0.05$; **$p < 0.01$; ***$p < 0.001$). Error bars indicate SEM.

(D) Immunofluorescence of TUBB3 (red), poly-E-T (green), or Δ2-T (blue) in human iPSC-neurons incubated at 4°C for 4 or 16 hr (n = 5 experiments from 2 cell lines). Note: Overexpression of *TUBB3* improved microtubule morphology only in the 4-hr cold-exposed group; Taxol is a known drug that binds and stabilizes microtubules. Low dose Taxol (0.1 μM) did not protect human iPSC-neuronal microtubules following 16-hr cold exposure. Scale bar: 40 μm.

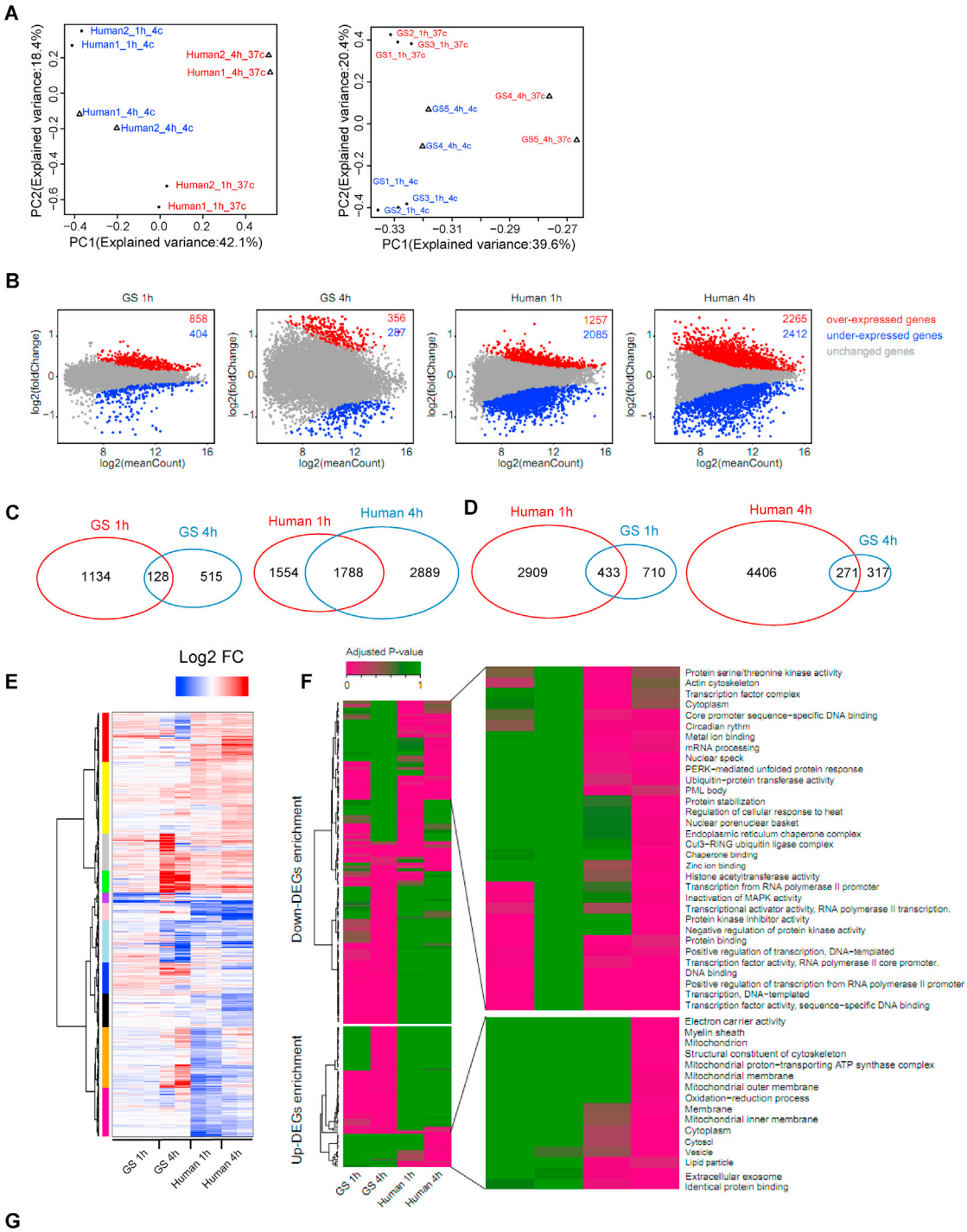


**Figure S3. Bioinformatics Analyses on GS and Human iPSC-Neurons, Related to Figure 2**

(A) Factorial map of the principal-component analysis (PCA) of scaled mRNA RPKM values. Top variant mRNAs were used. The proportion of the variance explained by the principal components is indicated in parentheses.

*(legend continued on next page)*

(B) M-A plots showing changes in gene expression in GS and human iPSC-neurons. M: $log_2$ mRNA fold change, A: $log_2$ mean values of gene-counts normalized by library size. Red dots: significant upregulated genes with adjusted $p < 0.05$; blue dots: significant downregulated genes with adjusted $p < 0.05$. Colored numbers in upper right correspond to the number of DEGs (upregulated: red; downregulated: blue).
(C) Venn diagrams indicating DEG overlap between the two time-points in human and squirrel.
(D) Venn diagrams indicating DEG overlap between human and squirrel orthologs at the two time-points.
(E) Clustering analysis of DEG orthologs with expression fold change. Sub-clusters are colored in red (785 genes), yellow (1150), gray (598), green (359), purple (167), pink (278), sky-blue (682), blue (499), black (549), orange (971), and claret (785) (top to bottom). $Log_2$ of DEGs fold change was used.
(F) Cell condition-based functional enrichment of DEGs in human and GS. The significance of enrichment is colored ranging from magenta (significant) to green (insignificant).
(G) An example of TUBB3 predicted acetylation sites. TUBB3 protein sequences from human, mouse, rat and GS (ICTTR) were aligned. Identical amino acids in the same corresponding positions of multiple alignments are colored in red.

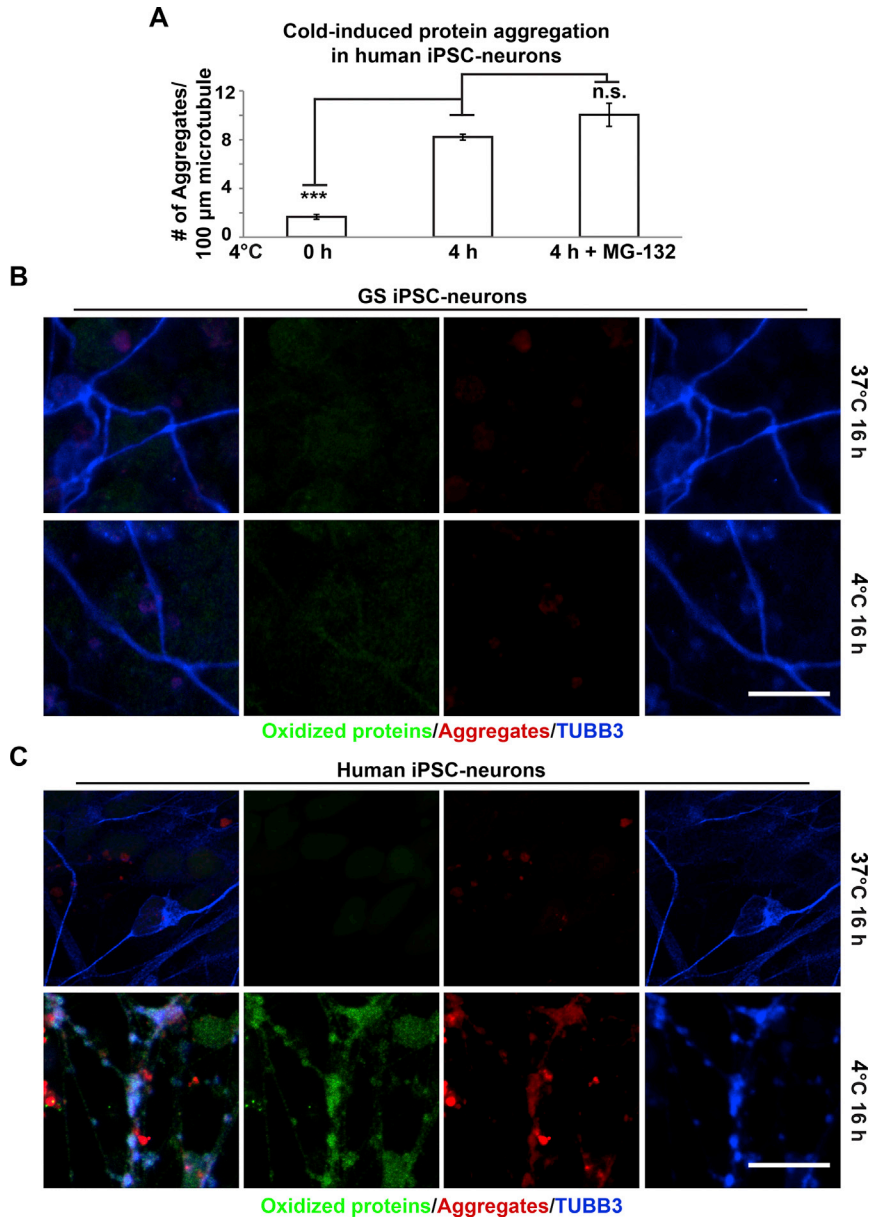


**Figure S4. Association of Protein Oxidation and Aggregation on the Microtubules of Cold-Stressed Human iPSC-Neurons, Related to Figure 3**

(A) In human iPSC-neurons, incubation at 4°C for 4 hr was sufficient to cause accumulation of protein aggregates along the microtubule processes, while pre-incubation with MG-132, a proteasome-specific inhibitor known to induce cellular protein aggregate formation, did not show any further increase in aggregation (n = 8 experiments for each group from 3 cell lines; ANOVA plus post hoc Tukey test for multiple cold-exposed groups treated for the same duration; n.s. not significant; ***$p < 0.001$). This result is consistent with our finding that in human iPSC-neurons vasolin-containing proteins (VCPs) and chaperone proteins (HSPs) that regulate ubiquitin-mediated protein degradation were downregulated at 4°C (Figure S5), compromising the delivery of damaged proteins via VCP to proteasomes. Error bars indicate SEM.

(B) Immunofluorescence of TUBB3 (blue), oxidized proteins (green) and a protein aggregate-binding dye (red; see STAR Methods) in GS iPSC-neurons (n = 5 experiments from 2 cell lines). Scale bar: 20 µm.

(C) Immunofluorescence of TUBB3 (blue), oxidized proteins (green), and a protein aggregate-binding dye (red) in human iPSC-neurons (n = 6 experiments from 3 cell lines). Scale bar: 20 µm.

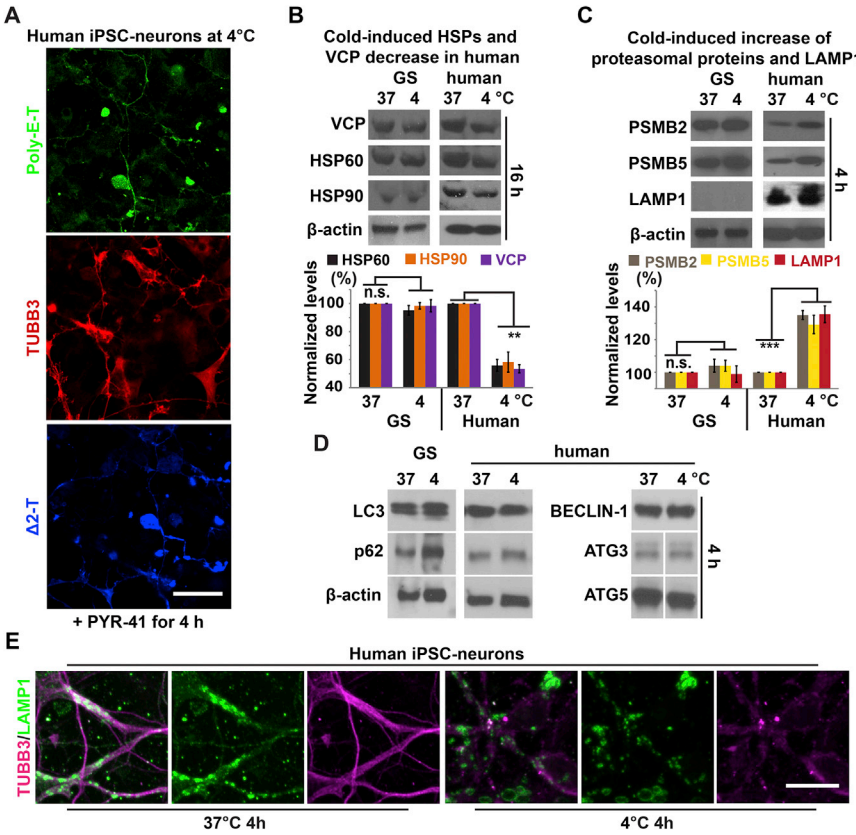


**Figure S5. Evaluating Key Components of the PQC System in Cold-Stressed Human iPSC-Neurons, Related to Figure 4**

(A) Pre-treatment with PYR-41, an inhibitor of protein ubiquitination did not improve microtubule morphology (poly-E-T: green; TUBB3: red; Δ2-T: blue) during 4-hr incubation at 4°C (n = 6 experiments from 3 cell lines). Scale bar: 30 μm.

(B) Western blots and quantification of valosin-containing protein (VCP) and molecular chaperones (HSP60 and HSP90) in human and GS iPSC-neurons after 16-hr incubation at 4°C (n = 5 experiments for each group from 2 GS and 2 human iPSC lines; Student's t test for two-group comparisons; n.s. $p > 0.05$, not significant; **$p < 0.01$). Error bars indicate SEM.

(C) Western blots and quantification of proteasomal subunits PSMB2 and PSMB5, and lysosomal protein LAMP1 in human and GS iPSC-neurons after 4-hr incubation at 4°C (n = 5 experiments for each group from 2 GS and 2 human iPSC lines; Student's t test for two-group comparisons; n.s. not significant; ***$p < 0.001$). Note that the LAMP1 antibody used in this study did not recognized GS LAMP1 proteins, probably because the epitope of LAMP1 proteins in GS is masked by GS-specific glycosylation. Error bars indicate SEM.

(D) Representative western blots show that protein levels of key autophagosome components remained little changed in GS and human iPSC-neurons after 4-hr cold exposure (n = 5 experiments for each group from 2 GS and 2 human iPSC lines).

(E) Immunofluorescence of TUBB3 (magenta) and LAMP1 (green; lysosomal marker) show evidence of lysosomal localization on microtubule processes of human iPSC-neurons. Scale bar: 20 μm.

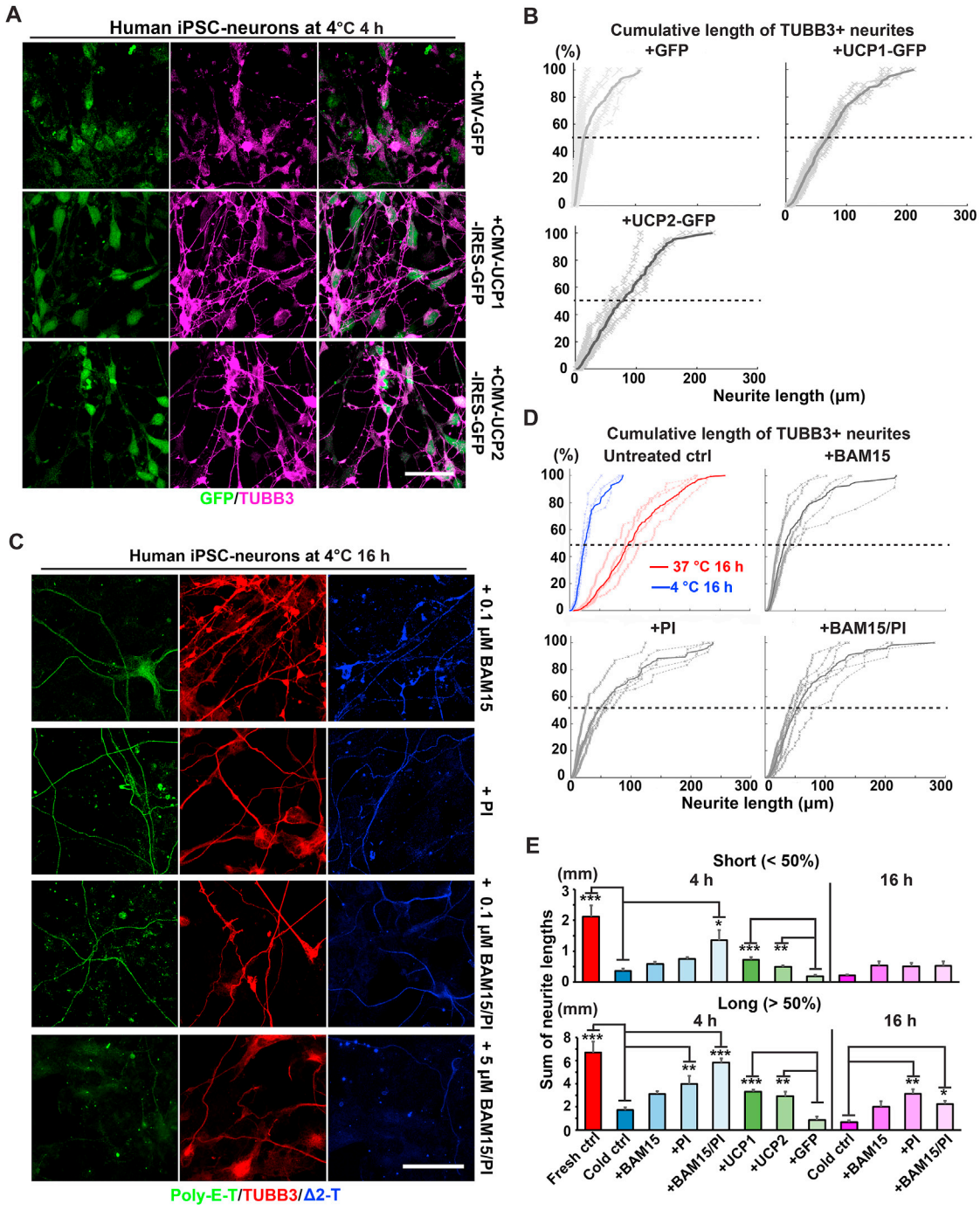


**Figure S6. Partial Preservation of Human iPSC-Neuronal Microtubules by Mitochondrial Uncoupling or PI against Cold Stress, Related to Figure 5**

(A) Immunofluorescence of TUBB3 (magenta) and GFP (green) in human iPSC-neurons transfected with plasmids overexpressing GFP only (*CMV-GFP*), UCP1 and GFP (*CMV-UCP1-IRES2-GFP*), or UCP2 and GFP (*CMV-UCP2-IRES2-GFP*) for 48 hr and then incubated at 4°C for 4 hr. Scale bar: 40 μm.

(B) Cumulative plots of TUBB3+ neurites of human iPSC-neurons following 4-hr cold exposure (n = 5 experiments from 2 cell lines for each group).

(C) Immunofluorescence of TUBB3 (red), poly-E-T (green), or Δ2-T (blue) in human iPSC-neurons incubated at 4°C for 16 hr. Note: High concentration of BAM15 (5 μM) produced poor microtubule morphology. Scale bar: 40 μm.

(D) Cumulative plots of TUBB3+ neurites of human iPSC-neurons (2 cell lines were tested; 0.1 μM BAM15: n = 6 experiments; 1:500 PI: n = 5 experiments; 0.1 μM BAM15 & 1:500 PI: n = 6 experiments) following 4- and 16-hr cold exposure.

(E) Quantification on the lengths of TUBB3+ neurites of human iPSC-neurons under different experimental conditions (Student's t test between untreated controls with or without cold exposure; ANOVA plus post hoc Tukey test for multiple cold-exposed groups treated for the same duration; *$p < 0.05$; **$p < 0.01$; ***$p < 0.001$). Error bars indicate SEM.

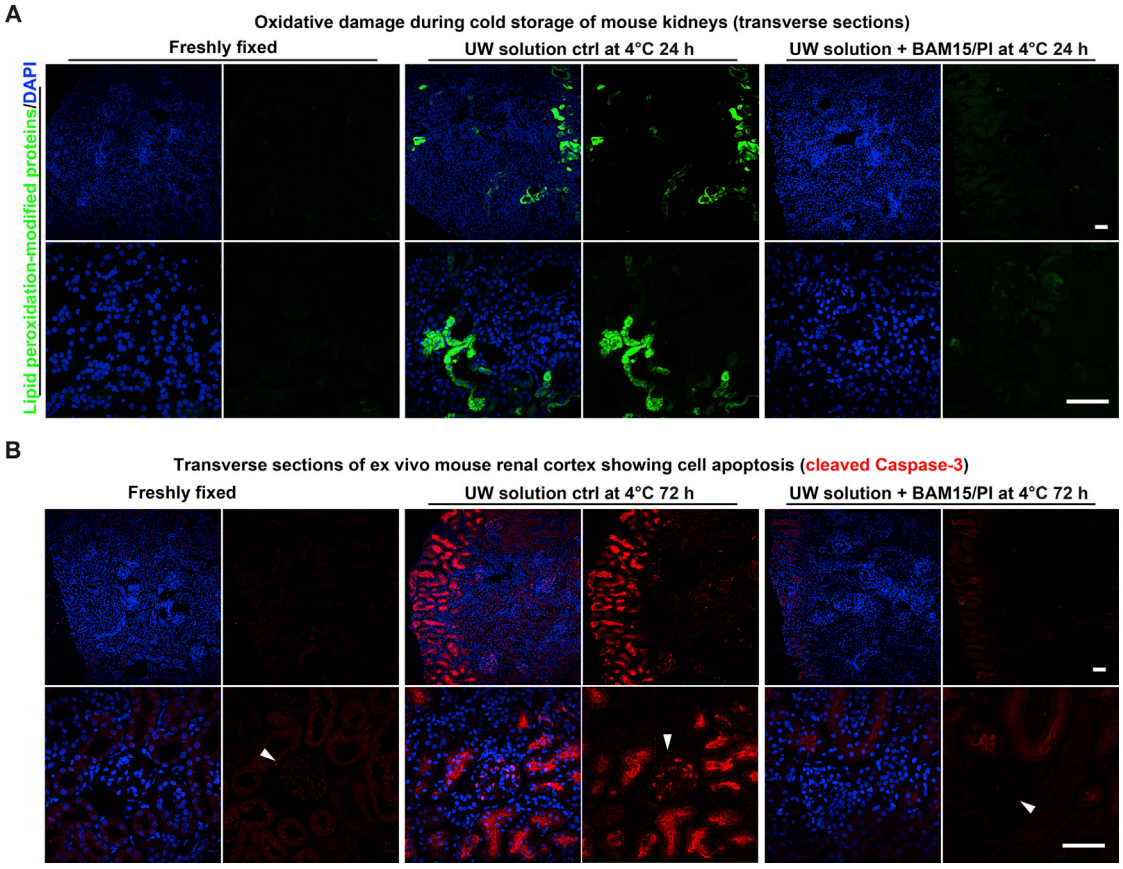


**Figure S7. Inhibiting Cold-Storage-Induced Lipid Peroxidation and Cell Apoptosis in Mouse Kidneys by BAM15/PI, Related to Figure 7**

(A) Kidneys from healthy wild-type mice were sectioned and visualized for proteins modified by lipid peroxidation (green; see STAR Methods; n = 4 animals in each condition). Scale bars: 50 μm.

(B) Immunofluorescence of an apoptotic cell marker, cleaved Caspase-3 (red), and DAPI (blue) in transverse sections of wild-type mouse kidneys under these conditions (n = 4 animals for each condition): freshly fixed and following 4°C 72-hr with or without BAM15/PI. Note that in the cold-exposed control group, high levels of cleaved Caspase-3 were found in the kidney cortex, including glomeruli (arrowhead). Scale bars: 50 μm.